



## Advanced Diagnostics in Oxy-Fuel Combustion Processes

**Brix, Jacob; Toftegaard, Maja Bøg; Clausen, Sønnik; Jensen, Anker Degn**

*Publication date:*  
2012

*Document Version*  
Publisher's PDF, also known as Version of record

[Link back to DTU Orbit](#)

*Citation (APA):*  
Brix, J., Toftegaard, M. B., Clausen, S., & Jensen, A. D. (2012). *Advanced Diagnostics in Oxy-Fuel Combustion Processes*. DTU Chemical Engineering.

---

### General rights

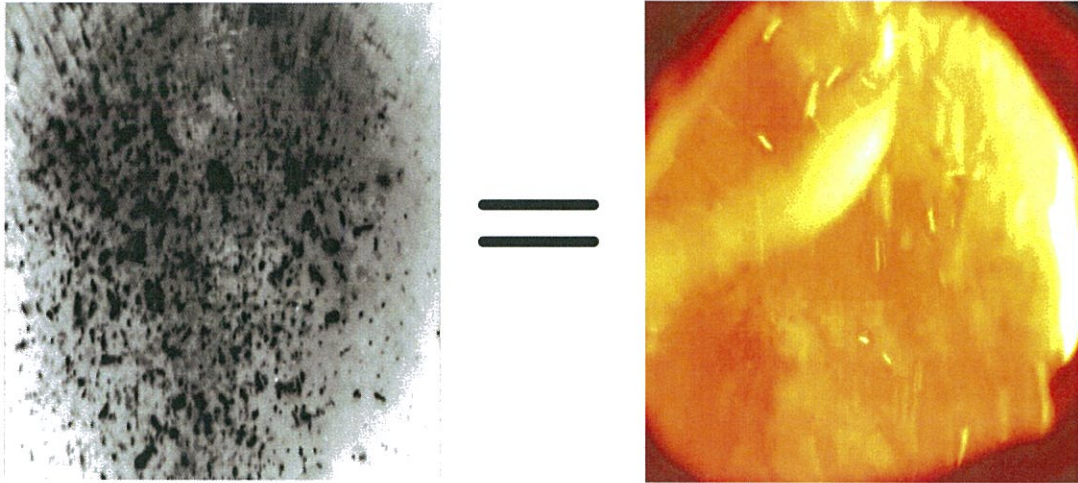
Copyright and moral rights for the publications made accessible in the public portal are retained by the authors and/or other copyright owners and it is a condition of accessing publications that users recognise and abide by the legal requirements associated with these rights.

- Users may download and print one copy of any publication from the public portal for the purpose of private study or research.
- You may not further distribute the material or use it for any profit-making activity or commercial gain
- You may freely distribute the URL identifying the publication in the public portal

If you believe that this document breaches copyright please contact us providing details, and we will remove access to the work immediately and investigate your claim.

# Advanced Diagnostics in Oxy-Fuel Combustion Processes

-The Use of IR and FTIR in Pilot- and Laboratory Scale Reactors-



## Final Report

Project No.: PSO-010069

## Authors

Jacob Brix<sup>1</sup>, Maja Bøg Toftegaard<sup>1,3</sup>, Sønnik Clausen<sup>2</sup> and Anker Degn Jensen<sup>1</sup>

<sup>1</sup>*Department of Chemical and Biochemical Engineering – Technical University of Denmark, Building 229 Søtofts Plads, 2800 Kgs. Lyngby, Denmark*

<sup>2</sup>*Department of Plasma Physics and Technology – Technical University of Denmark, Building 128, Fredriksborgvej 399, 4000 Roskilde, Denmark*

<sup>3</sup>*DONG Energy Power, Kraftværksvej 53, 7000 Fredericia, Denmark*

CHEC No. R1108

## **Preface**

This report describes the work carried out in the PSO project 010069 'Advanced Diagnostics in Oxy-Fuel Combustion Processes' in collaboration between the Department of Chemical and Biochemical Engineering and Risø National Laboratory for Renewable Energy. The project has been running in close collaboration with the PSO project 7171 'Oxy-Fuel Combustion for Below Zero CO<sub>2</sub> Emissions', and further discussion of the results presented in this report can be found in the PhD thesis of Maja Bøg Toftegaard (OxyFuel Combustion of Coal and Biomass, Ph.D. Thesis, CHEC Research Centre – Technical University of Denmark, 2011) as well as the final report of PSO 7171.

The project team would like to particularly thank research administrator of Energinet.dk Jesper Bergholdt Sørensen for a fruitful cooperation.

Front cover pictures:

Left: Thermal image of straw particles in first part of flame. Particles appear dark compared to the background (reactor wall) due to a comparably lower particle surface temperature.

Right: Image of flame taken with digital camera. Bright structures originate mainly from thermal radiation from soot.

## Resumé

Denne rapport beskriver resultaterne, der er blevet opnået i PSO-projektet 010069, “Advanced Diagnostics in Oxy-Fuel Combustion Processes”. Tre områder af optisk diagnostik er inkluderet i rapporten:

- FTIR målinger i en 30 kW swirlbrænder.
- IR målinger i en 30 kW swirlbrænder.
- IR målinger i en laboratorieskala fixed bed reaktor.

Resultaterne, der blev opnået i swirlbrænderen, viser at FTIR teknikken er et værdifuldt værktøj til bestemmelse af gasfasetemperaturer. Når dens anvendelighed evalueres sammenlignet med traditionelle termofølermålinger, må der dog skelnes mellem FTIR målinger udført med og uden kalot på proben. Når FTIR proben bruges med henblik på koncentrationsbestemmelse af gasfasekomponenter, skal der benyttes en kalot, der begrænser målingen til en fastlagt vejlængde. Når kalotten, der er kølet, er monteret på proben virker den afkølede på gassen og evt. forstyrrende på flammen, hvorfor temperaturmålingen bliver misvisende lav. Dette problem skyldes højst sandsynligt, at mindre flammer er mere påvirkelige for forstyrrelser end ved anvendelse af teknikken på fuldskala-flammer, hvor dette problem ikke ses. Når teknikken skal bruges til bestemmelse af gasfasetemperaturer, kan der derfor ikke måles koncentrationer samtidig. Bruges proben uden kalot, er resultaterne for temperaturmåling dog mere retvisende end termofølermålinger, der giver resultater på linje med FTIR målinger udført med kalot.

Anvendeligheden af FTIR teknikken til bestemmelse af koncentrationer af  $\text{H}_2\text{O}$ ,  $\text{CO}_2$  og  $\text{CO}$  viste en høj grad af præcision, selv om teknikken ikke er fuldstændig nøjagtig. Nøjagtigheden er afhængig af ensartetheden mellem koncentrationerne, der måles, og dem brugt til skabelse af de referencespektra, der bruges i datafortolkningen. Dette skyldes at transmittans ikke er en lineær funktion af koncentration. Stabiliteten af målingerne er også afhængig af den vejlængde der bruges. Fortolkningen af det målte optiske signal forudsætter perfekt opblanding, og en lille vejlængde, gør derfor at strømningsfænomener og opblandingsbegrænsninger ses som, til tider, store fluktuationer, når målingen laves over tid. Fluktuationerne er imidlertid udtryk for de faktiske forhold der findes i reaktoren, og er derfor en styrke ved metoden sammenlignet med ekstraktive metoder hvor der oftest opnås en betydelig grad af udjævning af signalet.

Anvendelsen af IR-teknikken til at bestemme partikelstørrelse, partikeltemperatur og partikelkoncentration viste sig som en god og pålidelig måde at opnå data på, både i swirlbrænderen og fixed bed laboratorieskala-reaktoren. Når teknikken blev brugt i swirlbrænderen var den efterfølgende databehandling dog i en vis grad følsom overfor optiske forstyrrelser i billederne, såsom tætte partikelskyer og slørede områder pga. høj partikeltæthed, der ind i mellem fejlagtigt blev fortolket som store enkeltpartikler af softwaren. Dette kan dog undgås i fremtidige studier ved at sætte skrapere kriterier til softwarens måde at behandle rådataene på. I fixed bed laboratorieskala reaktoren viste brugen af IR teknikken sig at være et særdeles værdifuldt værktøj i diskussionen og fortolkningen af eksempelvis NO data, målt med gasanalysatorer, og teknikken muliggjorde blandt andet bestemmelse af udbrændingstider i  $O_2/CO_2$ , hvor den høje  $CO_2$  koncentration ellers gør, at kulstofbalancen ikke kan bruges til formålet.

Igennem projektet har dataene været præsenteret i conferenceøjemed, dannet basis for en artikel samt blevet inkluderet som en vigtig del af to Ph.d. projekter. Disse aktiviteter er anført nedenfor.

- Joint Meeting of the Scandinavian-Nordic and French Sections of the Combustion Institute, Combustion of Char Particles under Oxy-Fuel Conditions: Formation of NO and Particle Temperature, Copenhagen, 9-10 November 2009.
- Brix J, Navascués LG, Joachim, Nielsen JB, Bonnek PL, Larsen HE, Clausen S, Glarborg P, Jensen AD, Oxy-Fuel Combustion of Coal Char: Particle Temperature and NO Formation, Submitted to Fuel on the 19<sup>th</sup> of November 2010.
- Brix J, Oxy-Fuel Combustion of Coal, Ph.D. Thesis, CHEC Research Centre – Technical University of Denmark, 2011.
- Toftegaard, MB, OxyFuel Combustion of Coal and Biomass, Ph.D. Thesis, CHEC Research Centre – Technical University of Denmark, 2011.

Yderligere er der gennemført to studenterprojekter i forbindelse med projektet:

Bonnek, PL og Nielsen, JB, 2\*20 point BSc projekt

Navascués LG, 30 point MSc projekt.

## Summary

This report sums up the findings in PSO-project 010069, “Advanced Diagnostics in Oxy-Fuel Combustion Processes”. Three areas of optic diagnostics are covered in this work:

- FTIR measurements in a 30 kW swirl burner.
- IR measurements in a 30 kW swirl burner.
- IR measurements in a laboratory scale fixed bed reactor.

The results obtained in the swirl burner have proved the FTIR method as a valuable technique for gas phase temperature measurements. When its efficacy is evaluated against traditional thermocouple measurements, two cases, with and without probe beam stop, must however be treated separately. When the FTIR probe is operated with the purpose of gas phase concentration measurements the probe needs to operate with a beam stop mounted in front of it. With this beam stop in place it was shown that the measured gas phase temperature was affected by cooling, induced by the cooled beam stop. Hence, for a more accurate determination of gas phase temperatures the probe needed to operate without the beam stop. When this was the case, the FTIR probe showed superior to traditional temperature measurements using a thermocouple as it could measure the fast temperature fluctuations. With the beam stop in place the efficacy of the FTIR probe for gas temperature determination was comparable to the use of a traditional thermocouple.

The evaluation of the FTIR technique regarding estimation of gas phase concentrations of  $\text{H}_2\text{O}$ ,  $\text{CO}_2$  and  $\text{CO}$  showed that the method is reliable though it cannot be stated as particularly accurate. The accuracy of the method is dependent on the similarity of the reference emission spectra of the gases with those obtained in the experiments, as the transmittance intensity is not a linear function of concentration. The length of the optical path also affects the steadiness of the measurements. The length of the optical path is difficult to adjust on the small scales that are the focus of this work. However, interpretation of the optic signal in terms of concentration, is done assuming a homogeneous mixture and so a small optic path length induces fluctuations in the measurements caused by flow phenomena (eddies and turbulent structures) as well as mixing limitations. The fluctuations, however, reflect the actual conditions in the reactor and so may be considered a strength of the method compared to extractive methods where the signal is most often evened out due to mixing in the sampling equipment.

The use of the IR technique for determination of particle temperatures, particle sizes, and number density proved reliable in both the swirl burner and the laboratory scale fixed bed reactor. When the technique was used in the swirl burner the subsequent data treatment was sensitive to optical disturbances, such as very dense particle clouds and blurred areas, which were sometimes mistakenly interpreted as particles by the software. This short come can however be avoided in future investigations by setting stricter identification criteria in the software. In the fixed bed reactor the use of the IR technique was an invaluable tool in the discussion of data obtained by gas analysis, and it allowed for estimation of combustion times in  $O_2/CO_2$  where the high  $CO_2$  concentration prevents the use of the carbon mass balance for that purpose.

During the project the data have been presented at a conference, formed the basis of a publication and it is part of two PhD dissertations. The name of the conference the journal and the dissertations are listed below.

- Joint Meeting of the Scandinavian-Nordic and French Sections of the Combustion Institute, Combustion of Char Particles under Oxy-Fuel Conditions: Formation of NO and Particle Temperature, Copenhagen, 9-10 November 2009.
- Brix J, Navascués LG, Joachim, Nielsen JB, Bonnek PL, Larsen HE, Clausen S, Glarborg P, Jensen AD, Oxy-Fuel Combustion of Coal Char: Particle Temperature and NO Formation, Submitted to Fuel on the 19<sup>th</sup> of November 2010.
- Brix J, Oxy-Fuel Combustion of Coal, Ph.D. Thesis, CHEC Research Centre – Technical University of Denmark, 2011.
- Toftegaard, MB, OxyFuel Combustion of Coal and Biomass, Ph.D. Thesis, CHEC Research Centre – Technical University of Denmark, 2011.

In addition two students projects have been carried out in relation to the project:

Bonnek, PL og Nielsen, JB, 2\*20 point BSc project

Navascués LG, 30 point MSc project.

## Table of Contents

1	The Swirl Burner Experiments .....	8
1.1	Solid Fuels and Experimental Conditions .....	12
2	Swirl Burner FTIR Measurements .....	16
2.1	Introduction .....	16
2.2	Instrumentation .....	18
2.3	The FTIR miniature probe .....	19
2.4	Data analysis .....	20
2.5	Gas Phase Temperature .....	25
2.6	Gas Phase Concentrations .....	33
3	Swirl Burner IR Measurements .....	38
3.1	In-Flame Measurements by Thermal Imaging .....	38
3.2	Theory and principles .....	38
3.3	Instrumentation .....	43
3.4	Data analysis .....	44
3.5	Particle Temperatures and Size Distributions .....	47
4	The Fixed Bed Experiments .....	54
4.1	The experimental Setup .....	54
4.2	Fuels and Char Preparation .....	56
4.3	Particle Temperatures and Burnout Times .....	57
5	Main Conclusions and Recommendations .....	65
6	References .....	67



## 1 The Swirl Burner Experiments

The down-fired swirl burner used during the experiments is shown schematically in figure 1. The combustion chamber is 1.9 m long, has a diameter of 0.315 m and is insulated by an 80 mm two-layer refractory lining and cooled by ambient air that flows in the void between the combustion chamber and the insulation shell.

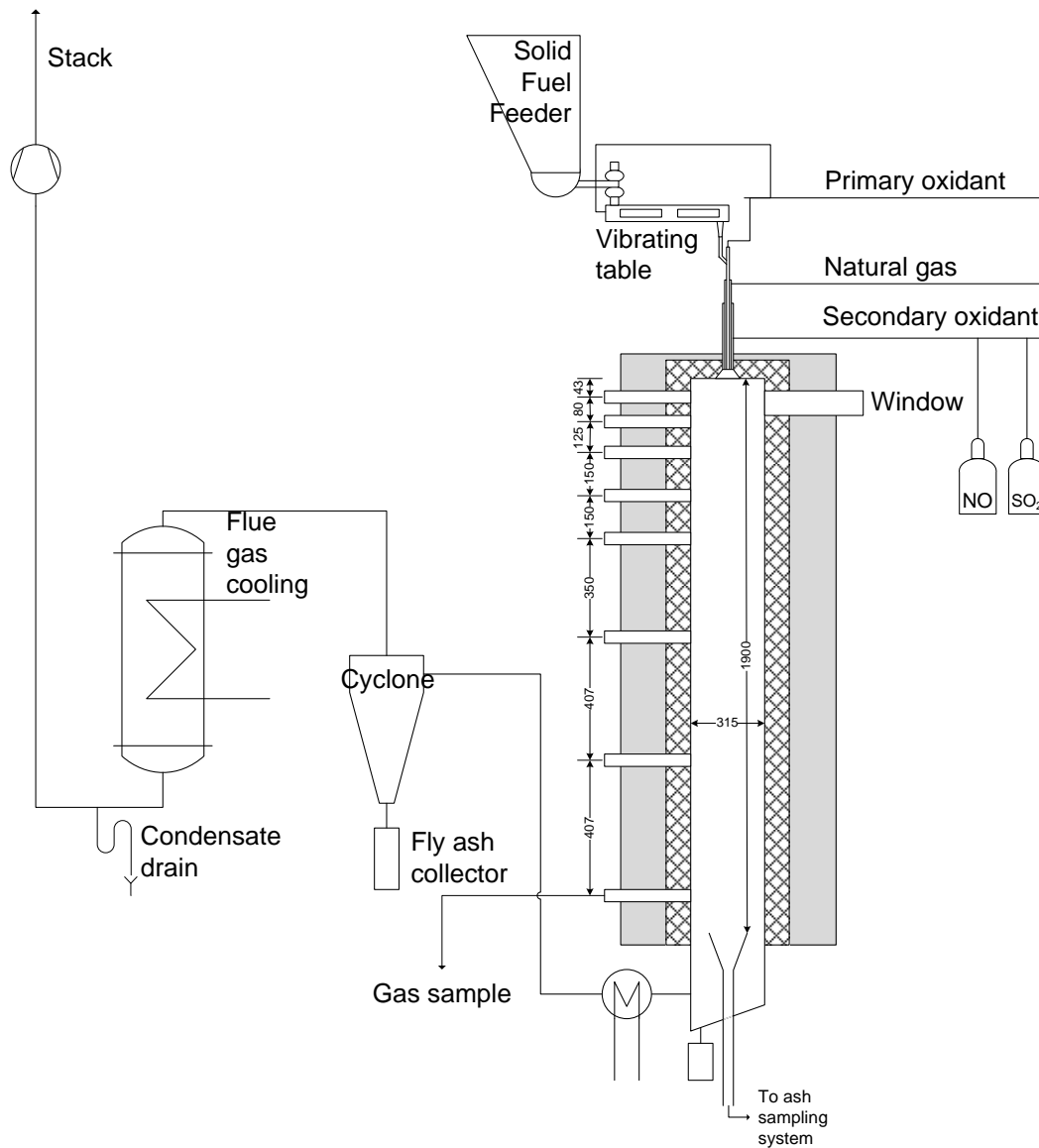


Figure 1 Schematic of the 30 kW swirl burner setup. All measures are in mm.

Through 8 ports in the reactor, numbered from the top and down, it is possible to conduct temperature mapping with e.g. thermocouples, insert measurement probes, collect gas samples etc. In this work the first 5 ports have been used for FTIR-measurements as it is this part of the chamber where the main part of the flame is located. Table 1 shows the distance from the burner to each port.

**Table 1 Distances from the burner at the five measurement ports.**

<b>Port</b>	<b>I</b>	<b>II</b>	<b>III</b>	<b>IV</b>	<b>V</b>
<b>Dist. Burner [mm]</b>	43	123	248	398	548

Fuel feeding is done using a twin-screw feeder, controlled by the recorded weight loss of the balance containing the fuel. The twin-screw feeder carries the fuel to a vibrating table that acts both as a conveyer belt and as a mean to dampen fluctuations in the feed rate. From the vibrating table the fuel reaches the central, primary burner tube where the primary oxidant is used for pneumatic transport of the fuel to the burner. A fraction of the primary oxidant is sent in already at the back end of the vibrating table to ease fuel feeding. The split in primary oxidant is adjusted before each experiment to ensure a stable feeding.

The top-mounted burner is shown schematically in figure 2. It consists of three tubes, two for primary and secondary oxidant and a separate, natural gas inlet which is used during reactor heat-up and during the transition to a solid fuel flame. The secondary oxidant is introduced in the burner in two separate streams, an axial flow and a tangential flow. The latter is responsible for creating a swirling motion and the swirl number is adjustable by choosing the ratio between the axial and tangential flow.

For both air and oxy-fuel experiments the primary oxidant flow is set at 20 vol. % of the total oxidant flow at the reference conditions. This implies that the linear velocity of the primary oxidant leaving the burner will differ when the combustion atmosphere and/or the stoichiometry is changed. However, the swirl number is kept constant to obtain similar conditions for air and oxy-fuel experiments.

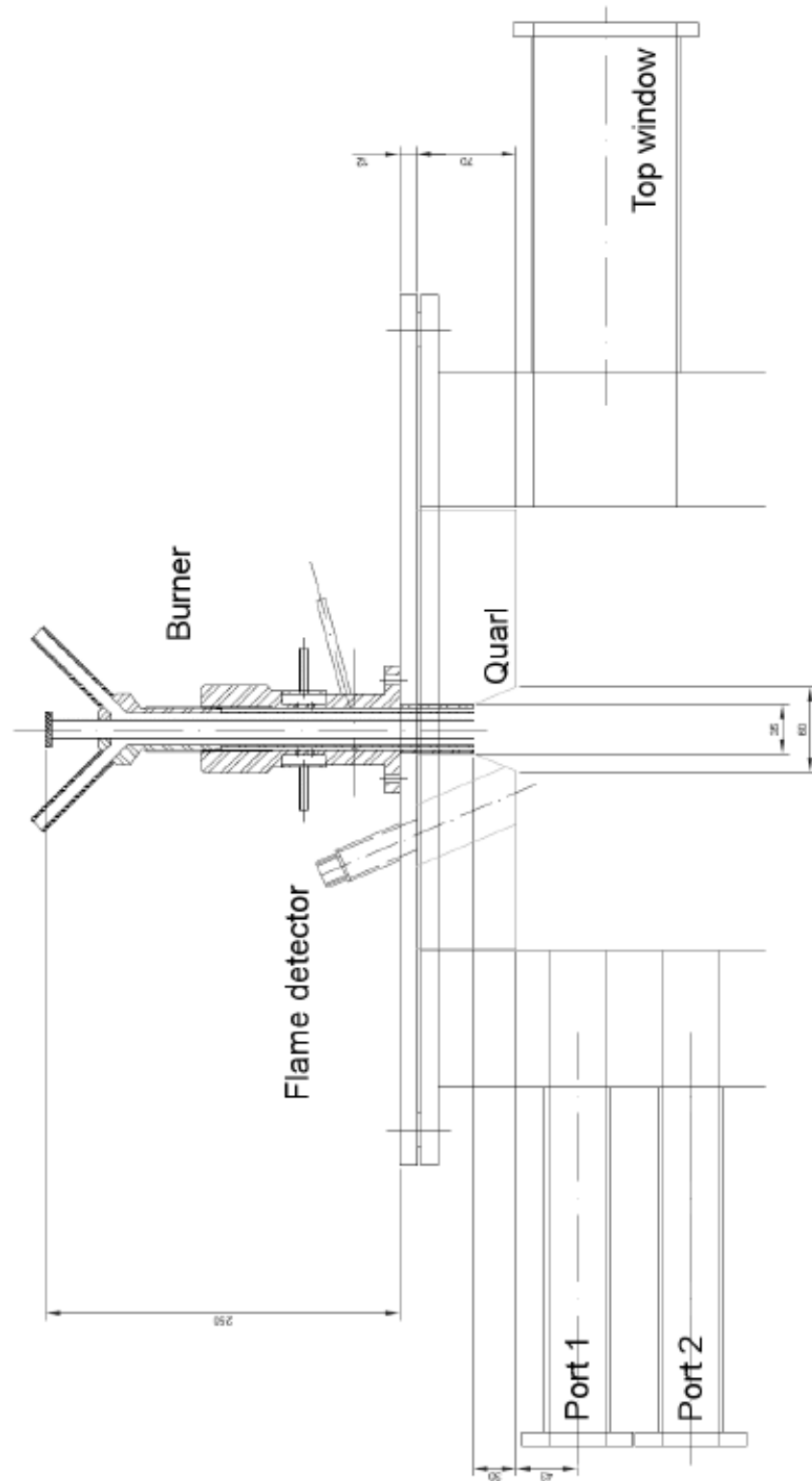


**Figure 2** The burner mounted on top of the combustion chamber. The sketch is rotated 45° due to limitations in page space.

The flow rate of the individual oxidant flows is controlled by manual valves and adjusted according to readings from rotameters. A more accurate monitoring of the total, oxidant flow rate is performed by mass flow controllers in the oxidant mixing panel. The mass flow controllers are likewise responsible for correctly mixing the oxidant for oxy-fuel experiments according to settings which are controlled in Labview.

The combustor is heated by natural gas combustion over-night or for at least 14 hours before an experiment starts in order to achieve stable temperatures of the reactor lining. For oxy-fuel combustion experiments the oxidant is switched to an  $O_2/CO_2$  mixture before the solid fuel feeding is started. After a minimum of 1 hr with pure solid fuel combustion the combustion chamber temperature profile, as well as the flue gas composition, has stabilized and the measurements and sampling can be initialized.

The reactor is a once-through type reactor and thus has no ducts for recirculation of flue gas in oxy-fuel operation.  $O_2/CO_2$  mixtures are produced at chosen molar ratios from gas bottles in the oxidant mixing panel. The primary and secondary oxidant flows are of the same composition. For air combustion the oxidant is supplied as pressurized, ambient air. Temperature measurements with an S-type thermocouple have been performed for all of the experiments presented herein. For many of the temperature data points several measurements have been performed at a specific radial burner position in a specific port in experiments carried out under similar conditions. For these measurements it is possible to calculate standard deviations, which are shown in the graphs of this report. For thermocouple data points that have not been repeated it can be assumed that standard deviations are of the same order as the standard deviations shown for comparable measurement positions. When the thermocouple is used to map the temperature profile across the diameter of the combustion chamber, especially at port I and II, it crosses the flame. This crossing brings with it the effect of “flame holding”, which means that the probe facilitates a more attached and compact flame, when temperature measurements are carried out on the opposite side of the reactor from the ports. When the flame becomes more compact and attached its temperature increases and the temperature readings from the opposite side of the combustion chamber therefore yield “artificially” high values. The effect of flame holding is also present when the FTIR-probe is used for measurements (see section 2). Figure 3 visualizes the effect of flame holding for a coal

flame burning in air. In the figure it can be seen that a brighter more intense flame is formed when the probe crosses the burner mouth.

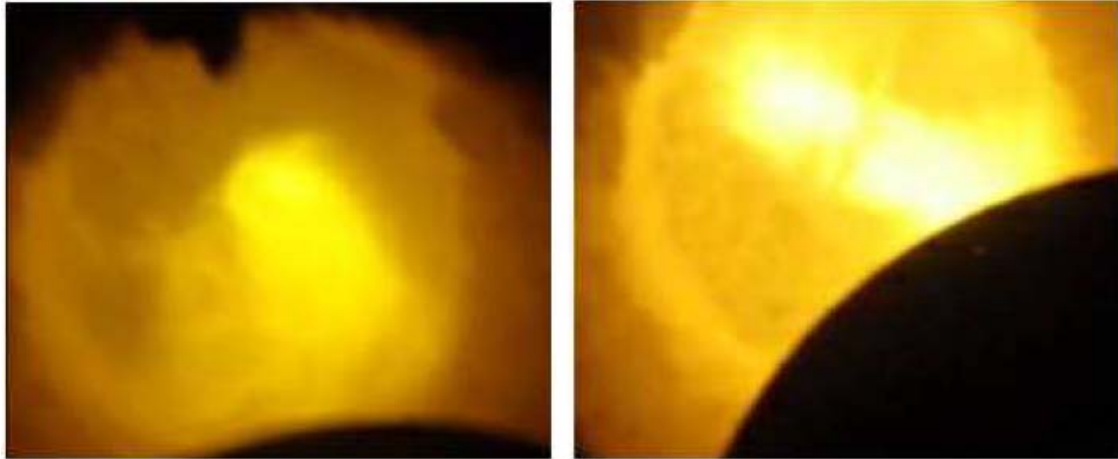


**Figure 3 Left: Coal/air flame. Right: Coal/air flame with thermocouple inserted across burner mouth.**

### **1.1 Solid Fuels and Experimental Conditions**

During the experiments two different fuels have been utilized, a Colombian bituminous coal from El Cerrejon (COCERR), and pulverized straw pellets made from cereal straw (wheat and barley in a non-specified ratio). The coal was delivered from the OxyCoal-UK project and was ground at delivery. The straw was delivered as pellets from Køge Biopillefabrik and pulverized with a specification of 100 % being below 700  $\mu\text{m}$ . The proximate and ultimate analysis of the fuels can be seen in table 2 and the cumulative particle size distributions are shown in figure 4. When the fuels are fired as a mixture containing 50 wt. % of each the thermal load is divided with 38 % from straw and 62 % from coal.

The mean particle size of the straw is generally much smaller than usually utilized when co-firing straw at low weight fractions in full-scale suspension-fired boilers. However, when biomass constitutes the major fraction of the fuel in suspension-fired boilers the particle size distribution is closer to the one used in the experimental setup. The main reason is the need for the biomass to aid in flame stabilization. When co-firing straw up

to about 20 wt. % the coal acts as the flame stabilizing element, which allows for larger biomass particles at these conditions.

**Table 2 Properties of El Cerrejón coal (Colombian) and cereal straw pellets (Danish).**

<b>Fuel</b>	<b>Coal</b>	<b>Straw</b>
<b>Heating Value (MJ/kg, ar)</b>		
LHV	27.09	16.40
<b>Proximate Analysis (wt. %, ar)</b>		
Moisture	5.03	5.10
Ash	9.62	4.40
Volatile	34.86	72.40
Fixed Carbon (by difference)	50.49	18.10
<b>Ultimate Analysis (wt. %, daf)</b>		
C	80.70	48.62
H	5.41	6.41
N	1.69	0.49
S	0.726	0.094
Cl	0.016	0.419
O (by difference)	11.46	43.97
<b>Ash Forming Element Composition (wt. %, dry)</b>		
Al	1.1	0.011
Ca	0.16	0.44
Fe	0.51	0.0076
K	0.18	1.00
Mg	0.14	0.054
Na	0.060	0.050
P	0.0078	0.062
Si	2.7	0.91
Ti	0.054	0.008
<b>Structural Properties</b>		
Bulk density (kg m <sup>-3</sup> )	1000	450
Particle diameter, median/d <sub>50</sub> (μm)	47	330

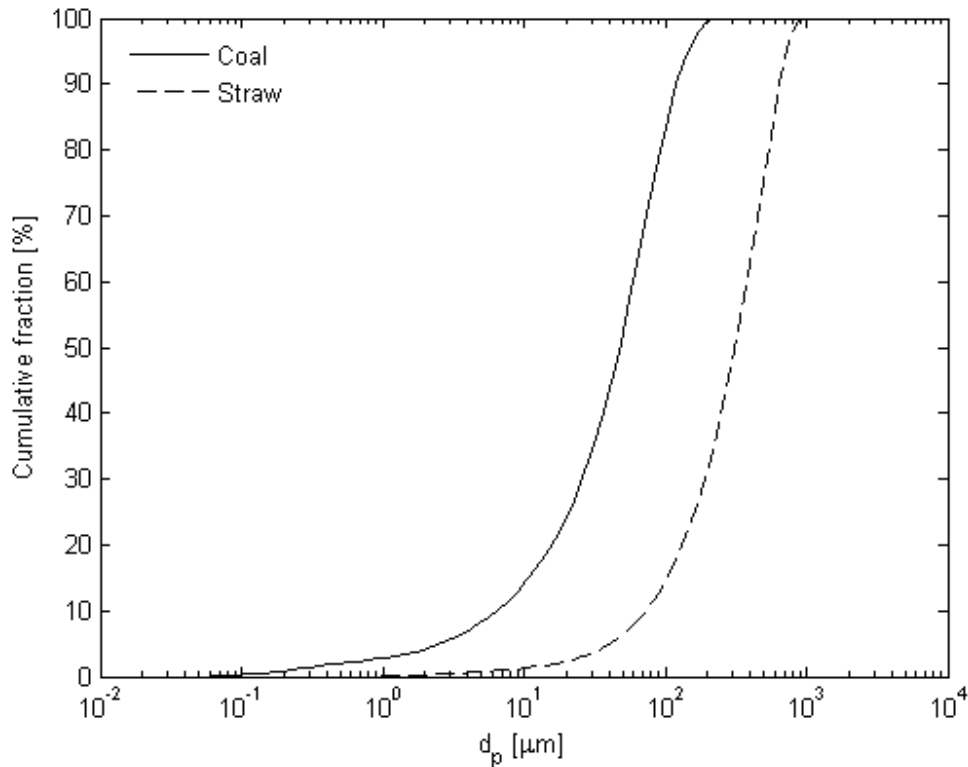


**Figure 4 Cumulative particle size distributions for coal and straw measured by a Malvern Mastersizer. The distribution type is volumetric.**

A total of six experimental series have been conducted for the purpose of FTIR and IR-measurements. The operational parameters during the experimental series are shown in table 3. It can be seen in the table that the  $O_2$  concentration under oxy-fuel conditions is 9 % pt. higher than in air and that the stoichiometric value of  $O_2$  is lower. The choice of  $O_2$  concentration of 30 vol. % during the oxy-fuel experiments has to do with flame stability. The lower flame propagation speed in  $CO_2$  and its higher heat capacity causes a cooler more unstable flame if the  $O_2$  concentration is significantly lower than approximately 30 vol. % [Toftgaard et al. 2010]. The stoichiometric value of  $O_2$ ,  $\lambda$ , is a result of the fixed entrance and exit concentrations at a constant thermal load (fuel feeding rate).

**Table 3 Overview of the operating parameters and their variations during the experimental campaign.**

<b>Air</b>	<b>Load</b>	<b>Fuel Flow</b>	<b>Inlet O<sub>2</sub></b>	<b><math>\lambda</math></b>	<b>Flue Gas exit O<sub>2</sub></b>	<b><math>\tau_{\text{average}}^*</math></b>	<b>Swirl Number</b>
	<b>[kW<sub>th</sub>]</b>	<b>[kg hr<sup>-1</sup>]</b>	<b>[vol. %]</b>	<b>[-]</b>	<b>[vol. %]</b>	<b>[s]</b>	<b>[-]</b>
<b>Coal</b>	30	3.99	21	1.3	5	2.7	1.8
<b>50 wt. % blend</b>	30	5.0	21	1.3	5	2.6	1.8
<b>Straw</b>	30	6.6	21	1.3	5	2.6	1.8
<b>Oxy-Fuel</b>							
<b>Coal</b>	30	3.99	30	1.19	5	3.9	1.8
<b>Straw</b>	30	6.6	30	1.22	5	3.7	1.8
<b>50 wt. % blend</b>	30	5.0	30	1.2	5	3.9	1.8

\*  $\tau_{\text{average}}$  is the average gas and particle residence time in the reactor



Since the flow of oxidant was controlled manually according to readings of rotameters deviations in stoichiometry from the values in table 3 up to app. 10 % was observed in the experiments. These small deviations do however not influence the accuracy of the FTIR and IR-measurements and they do not compromise comparisons between experiments as all experiments have been conducted at fuel lean conditions. Table 3 also shows average residence time of the gas and particles during the experiments. The residence time has been calculated using the actual measured reactor temperature profile (measured with thermocouple) and the theoretical flue gas flow. It is seen that reactor residence times are longer during oxy-fuel combustion, which is caused by the lower flue gas flow that is the result of the higher O<sub>2</sub> concentration at a constant thermal load.

## **2 Swirl Burner FTIR Measurements**

### **2.1 Introduction**

A Fourier Transform InfraRed spectrometer (FTIR-spectrometer) coupled to a water-cooled fibre-optic probe is a powerful tool for measurements of gas temperature and major gas components simultaneously from the thermal emission spectrum in flames and hot gases. Information about gas temperature and concentration fluctuations can be found from a number of single scan spectra that can provide representative mean values of the properties investigated. The method has been used previously in larger flames and boilers, [Clausen, 1996], [Bak & Clausen, 2002], [Yin et al., 2008], using an optical path length of approximately 250 mm and a probe diameter of typical 43 - 60 mm. The principle has been used recently in commercial measurement campaigns on 30 MW<sub>th</sub> oxy-fuel flames using a path length of 100 mm and a probe diameter of 50 mm at Vattenfall's facility in Schwarze Pumpe, Germany. The path length used is a determining parameter for the accuracy of the measurements, particular in air, as a longer path length with a higher number of e.g. CO<sub>2</sub> molecules will dampen the effect of fluctuations in gas phase concentrations due to e.g. feeding instability and mixing, especially when measurements are carried out close to the flame. When measurements are conducted under oxy-fuel conditions, the path length becomes less important (down to a certain limit) as the high CO<sub>2</sub> concentrations reduce the optic visibility.

Experimental instrumentation and data analysis methods in this work are similar to large scale measurements; however, a miniature measurement probe is needed to reduce disturbances from the probe itself during measurements in a laboratory scale reactor with a diameter of 315 mm. The optical path length is hence reduced from 100 mm to 30 mm to obtain local details in small oxy-fuel flames. The optical path length might be reduced further, but it will compromise the technique during practical operation and it is therefore not attempted in these measurements.

A special miniature fibre-optic FTIR-probe has been designed for measurements in the laboratory scale oxy-fuel flames in this work. The probe uses an optical path length of 30 mm and it has a diameter of 10 mm. The principle of the gas temperature measurements is described in [Clausen, 1996] and principles of the gas concentration measurements in [Bak & Clausen, 2002], but a short outline is given in the following sections along with a description of the measurement instrument and the method of data treatment.

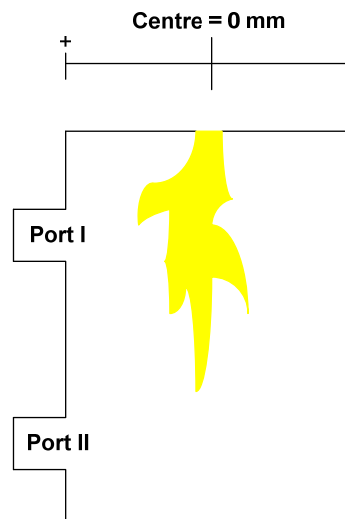


**Figure 5 Radial position index for measurements carried out across the reactor.**

In each port used for measurements, measurements have been carried out at different radial positions of the reactor. The indexing of the measurement positions are done by their distance from the burner centre according to figure 5. It can be seen in the figure that the radial distance becomes negative when the probe has crossed the centre of the reactor.

## 2.2 Instrumentation

The optical signal from the FTIR-probe is connected to the emission port of a FTIR-spectrometer of the type Bomem/ABB model MB155. The FTIR-spectrometer and FTIR-probe was purged with air from a compressor that was sent through a purge generator to remove  $\text{CO}_2$  and  $\text{H}_2\text{O}$  to avoid self-absorption effects and instabilities due to  $\text{H}_2\text{O}$  and  $\text{CO}_2$  in the ambient air.

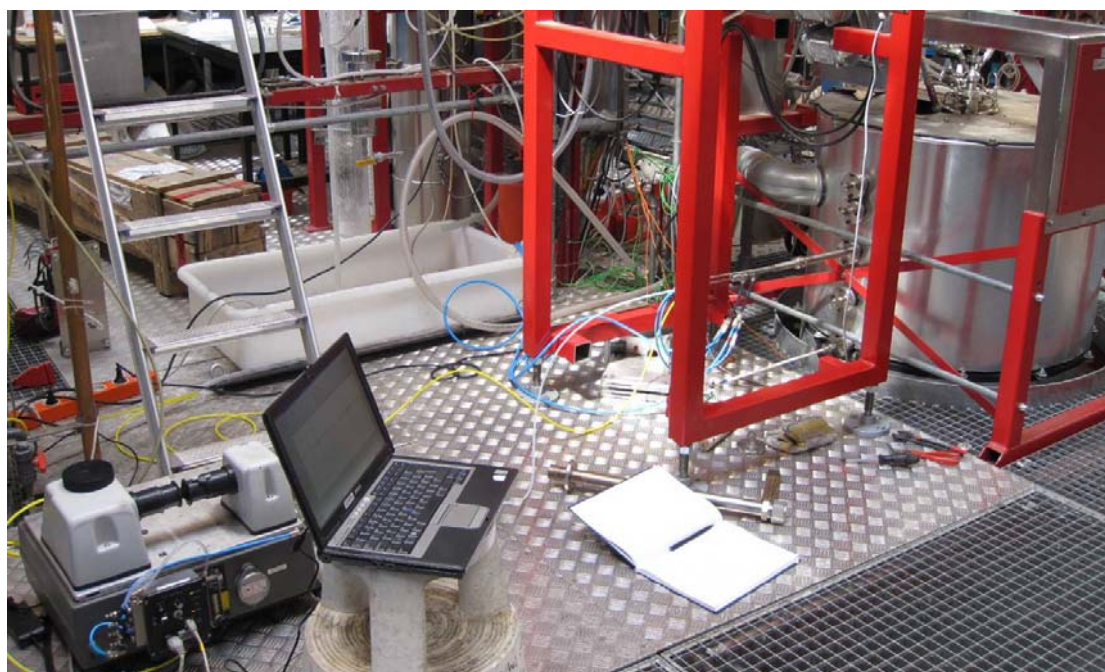


**Figure 6** Experimental setup with the FTIR-system (left in picture) and the top of the reactor (right). The top five ports of the reactor were mapped. The FTIR-probe is mounted at port 3 in this picture and the thermocouple at port 5 (close to the floor).

The FTIR-spectrometer was mounted with a sensitive liquid nitrogen cooled InSb-detector sensitive in the range  $1800 - 7000 \text{ cm}^{-1}$ . Approximately 60 double-sided single scan spectra per minute could be obtained with a spectral resolution of  $2 \text{ cm}^{-1}$ , which gave time dependent concentration- and gas-phase temperature profiles, from which average concentrations and temperatures could be determined along with values of standard deviations. The high resolution meant that the absorption peaks in the spectra defining e.g. the presence of CO was sufficiently well defined in the subsequent data treatment.

A notebook PC was used to control data acquisition and store data during experiments. The system was calibrated before and after experiments with a portable blackbody source, model R800 (Risø), with an uncertainty of  $\pm 3^\circ\text{C}$ . The setup with the FTIR-probe, the auxiliary equipment and the measurement ports can be seen in figure 6.

### 2.3 The FTIR miniature probe

A water-cooled, stainless steel probe was designed and built for measurements in the laboratory-scale oxy-fuel flames. Visualizations of the probe along with its dimensions can be seen in figure 7 and figure 8. The optical path (field of view in figure 8) is only 30 mm and the diameter of the probe with optics is only 10 mm. Cooling of the adjustable beam stop, which can be removed if desired, is provided by two 4 mm stainless steel tubes placed besides the probe with optics. A ceramic tube is mounted at the probe tip to reduce disturbances from the cold probe tip, particles in the flue gas and the preheated purge air. Thermal light from the hot slab of gas between the ceramic tip and beam stop is collected by a small 4 mm ZnSe lens focused on a IR-fibre connected to the FTIR-spectrometer by a SubMiniature version\_A (SMA) connector. All parts were designed, machined, mounted and tested at Risø DTU. A flow meter was used to control the purge flow around the optics and through the ceramic tip to avoid that dirty combustion gases and particles entered the probe tip. The purge flow was set as low as possible to minimize disturbances of the gas flow in the optic path. Experiments at different purge flow settings were carried out to investigate the effect on the measurements.



**Figure 7** The water-cooled fiber-optic probe for measurements of gas temperature and gas composition in the laboratory scale oxy-fuel flame. The FTIR-probe is inserted into a port holder with flange for leak tightness and easy handling during experiments.

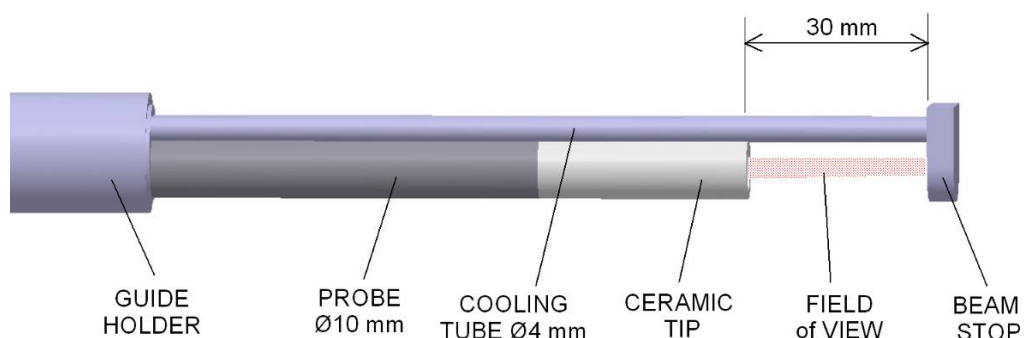


**Figure 8** Tip of the fiber-optic probe. Gas temperature and gas composition is measured along a 30 mm path between the beam stop and the front of the ceramic tip. Thermal light is collected with a 4 mm diameter ZnSe lens and focused on the end of a 550 $\mu$ m IR-fiber placed in the 10 mm water-cooled probe.



**Figure 9** Deposits on FTIR-probe after measurements in the flame. The first layer on water-cooled stainless steel probe is soot (black areas). A simple wire supports the mounting of the ceramic tube on the probe. Optics is placed 20-30 mm inside the probe from the tip of the ceramic tube.

When the FTIR-probe was inserted into the reactor, especially when placed close to the flame, soot and ash stuck to the probe and the beam stop, an example of which is shown in figure 9. For this reason the probe was often cleaned between experiments to avoid measurement inaccuracies due to changes in background (beam stop) texture and to avoid blockage of the optic path.

## 2.4 Data analysis

All experimental data is analyzed using array basic software running under GRAMS from Thermo. The program “ensted3\_multi\_auto\_cw6g.ab”, dated the 4<sup>th</sup> of June, 2010,

process data listed in batch jobs and write ascii-files with data time series and statistical results in a file for each port and measurement position. An example of an ascii-file with data time series can be seen in figure 10.

The first step in the data analysis, leading to ascii-files as that shown in figure 10, is to determine the gas temperature. The gas temperature can be found directly from the intensity of the  $2350\text{ cm}^{-1}$   $\text{CO}_2$  band using Planck's law with a calibrated system (blackbody reference) since the emissivity of that part of the  $\text{CO}_2$  band is 1.0 and therefore emits light like a blackbody, as visualized in figure 11. Since it is the emission signal from  $\text{CO}_2$  that is used to determine the gas temperature the signal needs to be strong enough for a temperature interpretation to take place. As the signal strength relates to the number of  $\text{CO}_2$  molecules on the optic path, measurements in air are carried out without beam stop to ensure a longer path length, and therefore an increased number of  $\text{CO}_2$  molecules.

It is generally assumed that the gas phase temperature is uniform over the 30 mm optical path. This assumption is not valid close to the burner outlet in the near burner zone where gas phase flow patterns are smaller than 30 mm and highly turbulent structures exist. Results obtained in the near burner zone (port I and II) should therefore be interpreted with care.

No.	Time	T_local	T_std	T_peak	T_3700	T_back	E_back	T_3.9	C_H2O %	CO2_2350 %	CO2%_3700 %	CO_ppm
1	58020.0	1278.4	4.3	1282.2	892.7	897.5	0.579	731.5	10.8	74.9	61.4	19830
2	58021.0	1316.9	8.1	1327.3	863.8	882.8	0.545	702.7	9.7	42.8	45.8	73670
3	58022.1	1222.0	5.7	1228.8	837.2	821.8	0.627	692.8	10.8	50.7	50.3	45580
4	58023.1	1402.7	10.0	1410.4	896.8	811.7	0.633	685.4	13.7	80.2	63.6	68795
5	58024.2	1270.0	5.4	1276.5	858.4	782.5	0.688	683.2	8.4	70.8	66.1	65598
6	58025.2	1289.7	8.3	1294.6	886.8	920.1	0.555	738.0	12.9	56.1	50.7	29107

**Figure 10** An example of a data time series from port III. Measurements are obtained at the burner centre during combustion of 50 wt. % straw and 50 wt. % coal in 30 vol. %  $\text{O}_2$  in  $\text{CO}_2$ . “No.” refers to the measurement number (1-60), “Time” is time the time of each measurement (0:00 = 0 seconds), “T\_local” is the local gas temperature just in front of the probes ceramic tip, “T\_std” is the standard deviation of “T\_local”, “T\_peak” is the highest gas temperature observed along the optical path, “T\_3700” is the gas temperature found from the  $3700\text{ cm}^{-1}$  emission band of  $\text{CO}_2$ , “C\_H2O %” is the  $\text{H}_2\text{O}$  content of the gas in vol. %, “CO2\_2350 %” is the wet  $\text{CO}_2$  concentration of the gas found from the  $2350\text{ cm}^{-1}$  band of the emission spectra, “CO2\_3700 %” is the wet  $\text{CO}_2$  concentration of the gas found from the  $3700\text{ cm}^{-1}$  band of the emission spectra and “CO\_ppm” is the wet CO concentration in ppm.



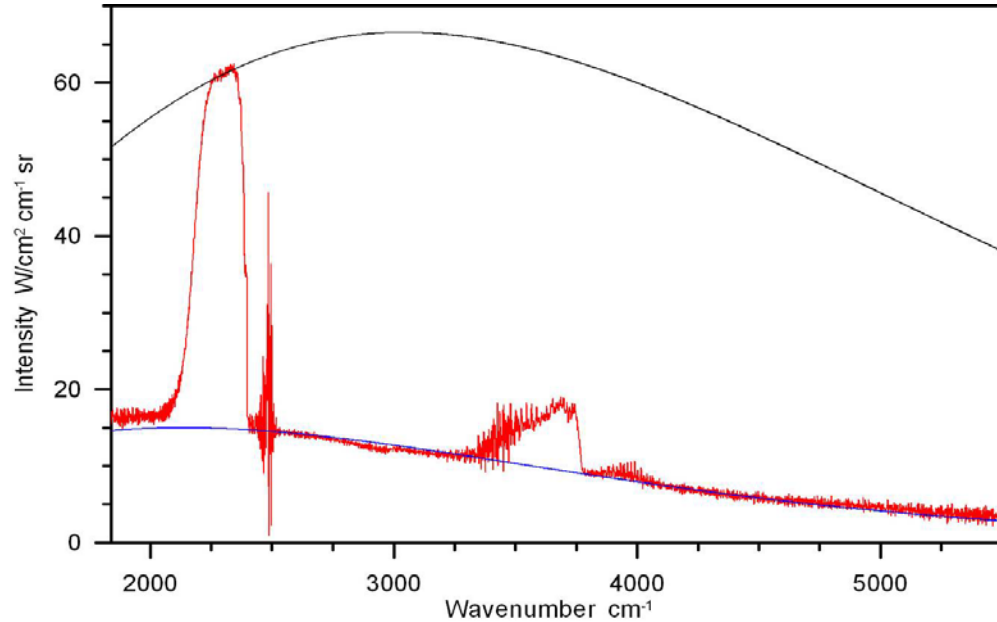


**Figure 11** Measured emission spectrum (red curve) at port III with the probe positioned at the burner centre. The data is from the same experimental series as in figure 10. Conditions at the measurement position:  $T_{\text{gas}} = 1277^{\circ}\text{C}$ , CO 83714 ppm (wet),  $\text{CO}_2$  60.2% (wet),  $\text{H}_2\text{O}$  10.4%. An emission spectrum of a grey body is fitted using Planck's law at a temperature of  $815.5^{\circ}\text{C}$  and an emissivity of 0.651 (blue curve). A black body emission spectrum is also fitted using the gas temperature (black curve). The noisy feature at  $2500\text{ cm}^{-1}$  in spectrum is due to a low signal in this region caused by absorption in the optical fiber.

The experimental transmittance spectrum is calculated from the emission spectrum as second step in the data analysis. A blackbody transmittance spectrum at the gas temperature and a transmittance spectrum of thermal radiation emitted from the background surfaces are needed. Thermal radiation from the background surfaces is fitted using Planck's law assuming a grey body, i.e. emissivities and temperatures of the surfaces (particles and beam stop) are determined by non-linear least square fits. The mean particle temperature and particle area density can in principle be found, but it requires great care in the optical design of the lens system, i.e. sufficient path length (100 – 250 mm) to obtain a strong enough signal and to ensure that thermal radiation from the beam stop is minimized (avoid deposits and black absorbing coating, see figure 9). Particle temperature measurements with the FTIR-probe are therefore not an issue in this work.

Third step in data analysis is the calculation of gas concentrations of selected species knowing the gas temperature. Knowing the gas temperature is essential as optical properties of gases vary with temperature. A look-up library of reference transmittance spectra based on hot gas cell measurements (CO<sub>2</sub>) and spectroscopic data base HITEMP (CO, H<sub>2</sub>O) calculations for different temperatures are used. Gas concentrations are found from the best match of scaled reference spectra with the experimental spectrum. Beer's law, shown in eq. 1 is used for scaling of reference data.

$$\tau(\nu, T) = e^{-a(\nu, T)lc} \quad \text{Eq. 1}$$

What Beer's law describes is the intensity,  $I$ , of electromagnetic radiation (light) as a function of initial intensity,  $I_0$ . The ratio between these two radiation intensities are shown as the transmittance,  $\tau(\nu, T)$ , in eq. 1. The transmittance is a function of radiation path length,  $l$ , an absorption coefficient,  $a$ , that is depending on the path media, the wave length of the radiation and the temperature as well of the concentration of the gas. When Beer's law is used to scale reference data down to a path length of 30 mm it interprets the radiation signal over a fixed traversed path length in the form of the number of molecules (concentration) that the signal encountered on its path. Because the use of Beer's law as a mean to interpret concentrations is locked to a specified path length species concentrations cannot be found from measurements in air, as these measurements are carried out without the beam stop to ensure a sufficiently strong CO<sub>2</sub> signal for gas temperature determination.

Gas spectra are analyzed using a set of reference data of CO at 1 vol. %, CO<sub>2</sub> at 8 vol. % and H<sub>2</sub>O at 10 vol. % for a path length of 250 mm in the temperature range 400-1600 °C, which is used in large scale FTIR flame measurements. Reference data are stored as spectrums with 2 cm<sup>-1</sup> of spectral resolution similar to the resolution of FTIR-spectrometer used in experiments.



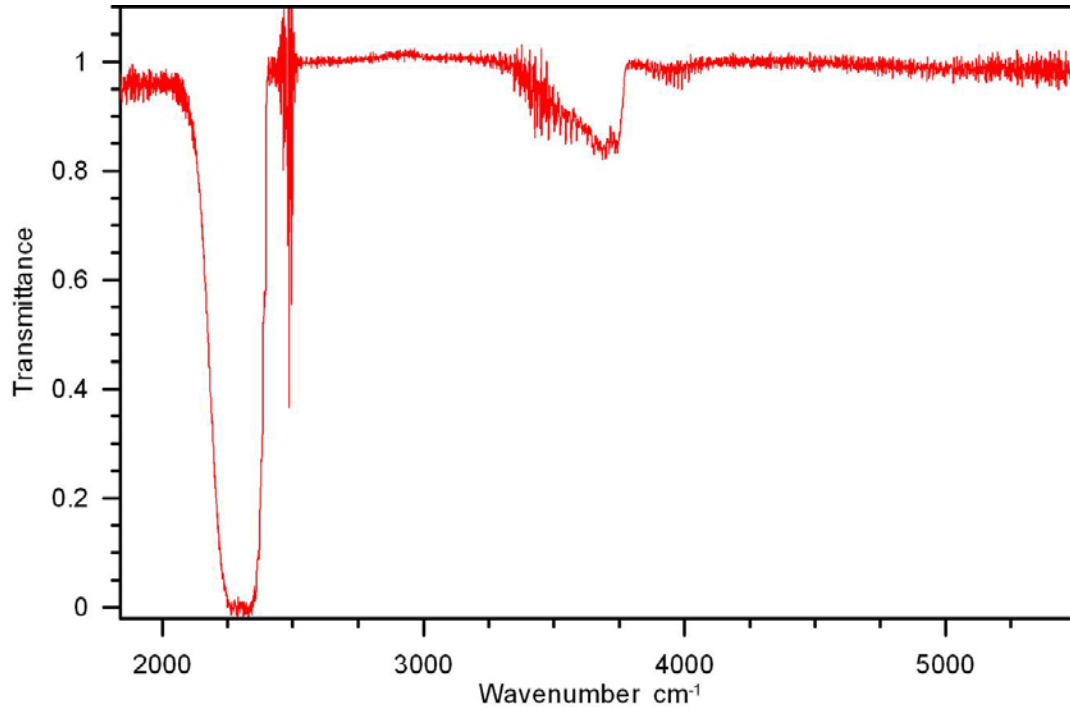


**Figure 12** Transmittance spectrum calculated from the emission spectrum shown in Figure 11 using information about grey body fit and gas temperature found from the CO<sub>2</sub> band at 2350 cm<sup>-1</sup>. The H<sub>2</sub>O content is found from the H<sub>2</sub>O band in the region 3800-4100 cm<sup>-1</sup>, the CO<sub>2</sub> concentration is found from the 3700 cm<sup>-1</sup> band and the CO concentration is found from the fine structure of CO in the 1950-2200 cm<sup>-1</sup> region.

The reference spectra corresponds to 8.33 vol. % CO, 66.7 vol. % CO<sub>2</sub> and 83.3 vol. % H<sub>2</sub>O when it is scaled for a path length of 30 mm. CO and CO<sub>2</sub> reference values is at a similar level as found in the reactor under oxy-fuel conditions, whereas the H<sub>2</sub>O reference value is significantly larger than encountered in the combustion chamber. The larger reference value for H<sub>2</sub>O might lead to a minor systematic error in the determined H<sub>2</sub>O concentration due to non-linearity. The shorter optical path length lowers the CO detection limit with a factor 8.33 to approx. 2500 ppm and the water band at 3800-4100 cm<sup>-1</sup> becomes weaker in the spectrum.

The concentration of CO<sub>2</sub> is calculated from two different bands, i.e. the CO<sub>2</sub> band at 2350 and 3700 cm<sup>-1</sup>. The 3700 cm<sup>-1</sup> band of CO<sub>2</sub> is the most accurate as the 2350 cm<sup>-1</sup> band requires highly uniform conditions along the optical path especially for oxy-fuel conditions. Therefore values marked "CO2\_3700\_%" in the ascii-files should be used. Figure 12 show an example of a transmittance spectrum from which concentrations of CO<sub>2</sub>, H<sub>2</sub>O and CO can be calculated using the reference spectrum.

## 2.5 Gas Phase Temperature

Figure 13 and figure 14 show gas-phase temperature profiles as given in the data time series in the ascii-files that is the output from data analysis (see section 2.4). Figure 13 shows the temperature profiles measured at port I across the diameter of the combustion chamber. In the experiment straw is fired under oxy-fuel conditions and the FTIR-probe is operated with the beam stop in place in front of the ceramic tip.

From figure 13 it can be seen that the temperature profiles fluctuate somewhat in time though the fluctuations takes place around a constant mean value. As discussed in section 2.4 measurements near the burner mouth can to some extent be influenced by the presence of gas-phase flow patterns, such as eddies, mixing limitations and highly turbulent structures, that take place on scales smaller than the optical path length of the probe. As an assumption for data treatment is a homogeneous gas phase environment throughout the optical path length these phenomena will cause inaccuracies during data interpretation. Another cause for fluctuations can be feeder instability, which will cause an unsteady flame structure and therefore changes in the FTIR-measurements, which do however, reflect actual conditions in the reactor. In figure 13 the effect of “flame holding” (see section 1) is clearly seen from the higher temperatures at the positions -30 and -60 mm where the probe has crossed the burner mouth.

Figure 14 shows gas-phase temperature profiles measured at the centre of the combustion chamber in ports I-V under the same conditions as in figure 13. Figure 14 shows a high degree of fluctuations at all the measurement ports. This indicates that the fluctuations seen in the profiles in both figure 13 and figure 14 cannot be explained solely by near flame phenomena such as eddies, mixing and highly turbulent structures but that overall system disturbances such as feeder instability also plays a role.

A probe purge flow of air was used to avoid that particles and combustion gases entered and deposited in the probe. As the presence of air in front of the ceramic tip of the probe is a possible source of error two different purge flows, one double the other, were tried in order to evaluate their effect on the measurements. The top graph of figure 15 shows the temperature profiles measured by the FTIR-probe using the two different purge flows along with the temperature profile measured with the S-type thermocouple.

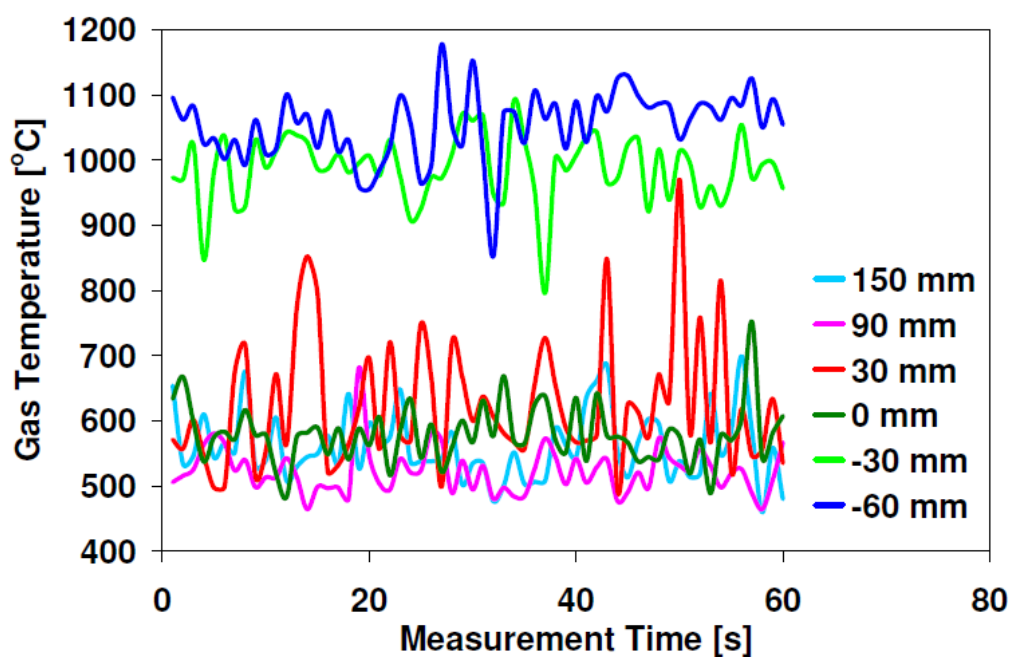


Figure 13 Gas phase temperature profiles measured during straw firing under oxy-fuel conditions. Measurements are conducted at port I with the beam stop in place in front of the ceramic tip of the FTIR-probe.

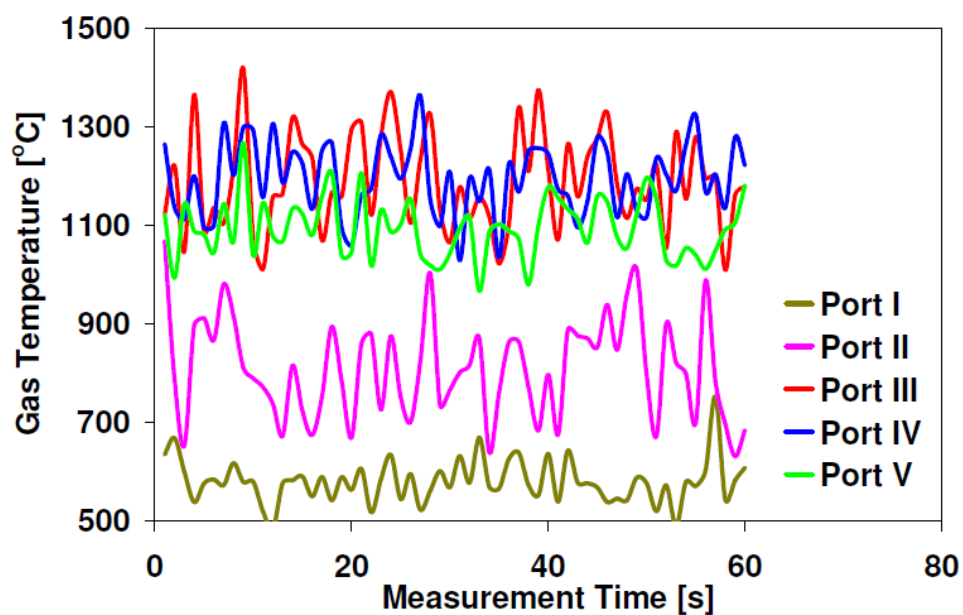


Figure 14 Gas phase temperature profiles measured during straw firing under oxy-fuel conditions. Measurements are conducted at the reactor centre (0 mm) at port I-V with the beam stop in place in front of the ceramic tip of the FTIR-probe.

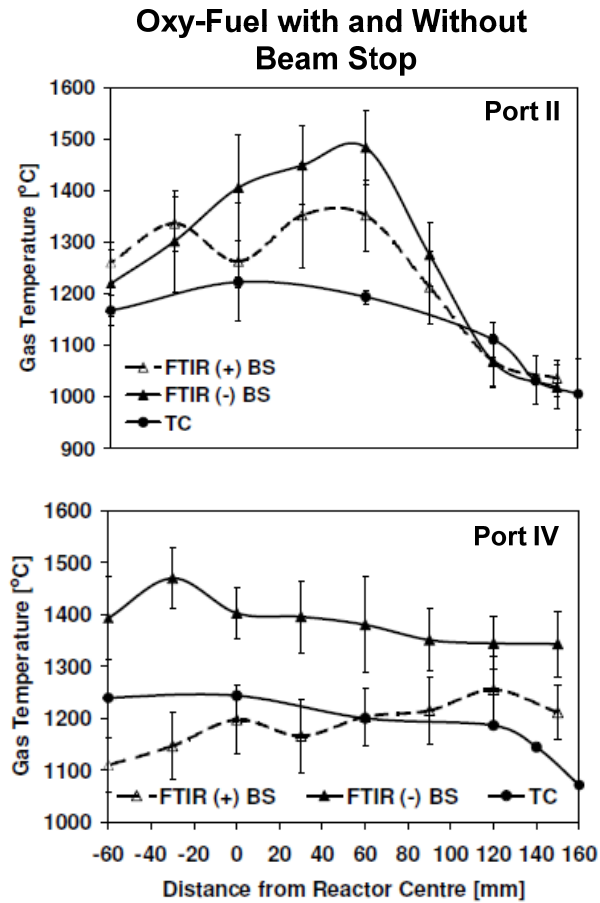
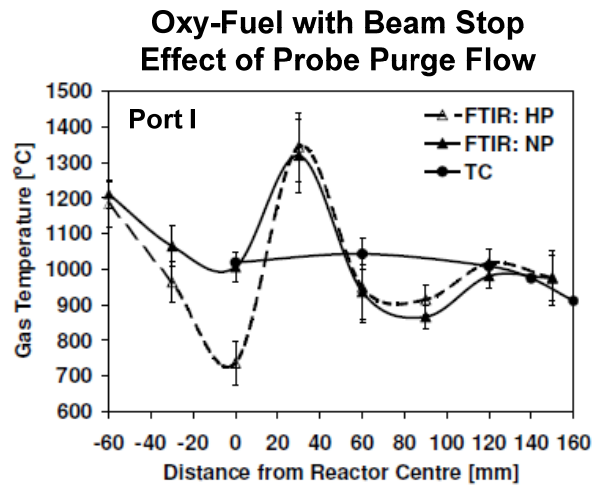


Figure 15 Temperature profiles measured by the FTIR-probe and the S-type thermocouple during coal fired experiments. NP = Normal purge flow, HP = High purge flow (2 x NP), BS = Beam stop, TC = Thermocouple.

It can be seen in the figure that the two FTIR-temperature profiles are fairly similar, reassuring that the low purge flow, used in all remaining experiments, did not contribute significantly to errors in the optic measurements. The deviation seen in the graph for measurements at the position 0 mm is not necessarily caused by the purge flow. As the measurements are carried out through port I and the position 0 mm corresponds to the probe in place just in front of the burner mouth feeder instability as well as flow and flame phenomena are likely sources of deviations.

The bottom two graphs of figure 15 show temperature profiles measured by the thermocouple and with the FTIR-probe, both with and without beam stop. It can be seen that a reasonable consistency is obtained between thermocouple- and FTIR-measurements when the probe is operating with the beam stop in place. When the beam stop is removed the FTIR-measurements tends to yield a higher gas temperature than compared to the other two profiles. The reason for the higher temperature lies in the cooling effect that the beam stop has when FTIR measurements are carried out with it in place. When temperature measurements are carried out with the thermocouple a strong radiation heat transfer with the cooled reactor wall will likewise cause lower temperatures. The radiation heat transfer during thermocouple measurements also means that this method cannot detect radial and time dependent temperature variations well. Of the temperature profiles shown in the two lower graphs of figure 15 the FTIR measurements without the beam stop can therefore be taken as the most representative of the actual conditions in the absence of measurement devices and shows the strength of the method.

In figure 16 FTIR- and thermocouple temperature profiles are shown for coal fired experiments under both air and oxy-fuel conditions. It can be seen that when coal is fired in air and FTIR-measurements are carried out without beam stop FTIR-temperature profiles are generally higher than the temperature profiles measured by the thermocouple, as discussed above. When coal is fired under oxy-fuel conditions and FTIR-measurements are carried out with the beam stop in place the temperature profiles measured with the FTIR-probe and the thermocouple are more in line. For both oxy-fuel- and air firing the differences between FTIR- and thermocouple measurements narrow as the distance from the burner mouth increases.

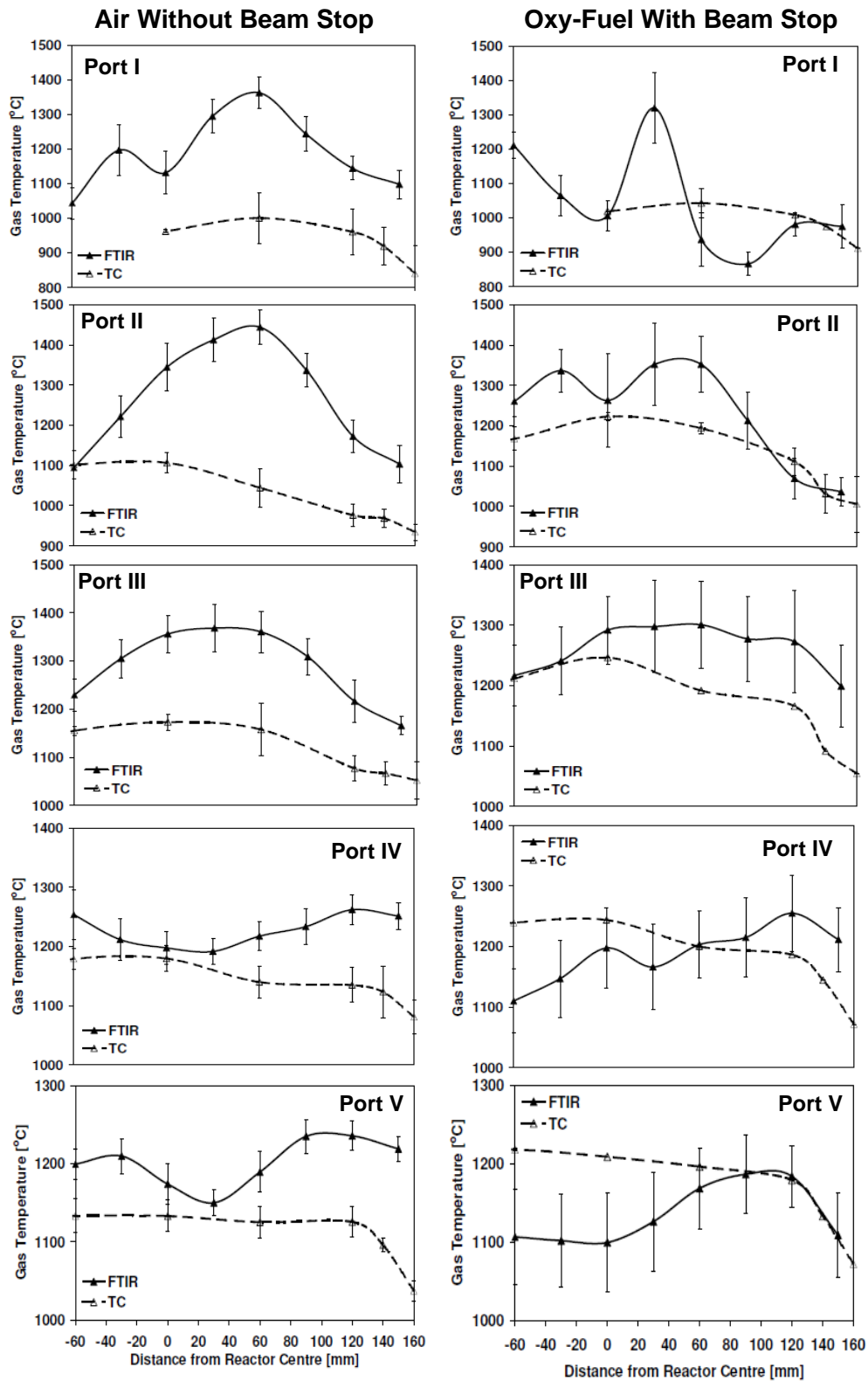


Figure 16 Temperature profiles measured by the FTIR-probe and the S-type thermocouple during coal fired experiments.

This is partly due to a more homogeneous gas phase, a lower degree of disturbances from flame and flow phenomena and a more even radial temperature profile, which makes the measurements less sensitive to mixing and small scale turbulent flow patterns. Also, the gas phase and reactor wall approaches thermal equilibrium, which means that the radiation heat transfer between the thermocouple and the wall causes a smaller error. Figure 16 suggests that the flame is not completely axis-symmetric but tends to be shifted towards the positive radial values (the side of the combustion chamber used for probe and thermocouple insertion). In port I and II the lack of flame symmetry are strongly influenced by factors such as flame holding caused by the probe, as discussed above.

Figure 17 shows FTIR- and thermocouple temperature profiles measured during oxy-fuel firing of straw. From especially the FTIR-measurements at port I and II the effect of flame holding is clearly seen. That the effect of flame holding seems more pronounced during straw firing in figure 17 than during coal firing in figure 16 has to do with the high volatile content of the straw compared to the coal (see table 2) and that the straw flame ignites further down the reactor than the coal flame (larger particles). Operating at the same thermal load under both coal and straw firing means that the significantly higher volatile content of the straw will result in a stronger heat release near the burner and therefore make probe measurements more prone to flame holding at port I and II. Besides port I, where the thermocouple has radiation heat exchange with the flame further down the reactor, figure 17 shows good consistency between FTIR and thermocouple measurements. As was the case in figure 16, figure 17 does not show a completely symmetric flame structure though this is hard to evaluate quantitatively from the figure.

Figure 18 shows FTIR- and thermocouple temperature profiles for experiments under both air and oxy-fuel conditions where a 50 wt. % mixture of straw and coal has been used as fuel. In this figure an effect of flame holding (artificially high temperatures when the probe has crossed the reactor centre) is also seen for port I, II and III though the effect is lower than in figure 17 where only straw was used as fuel. A reasonable consistency between the FTIR and thermocouple profiles is seen in figure 18 for oxy-fuel combustion when FTIR-measurements are carried out with the beam stop in place. The reasons for this were discussed above in connection to figure 15. As it was also the case in figure 16 and figure 17, the profiles in figure 18 show a higher degree of mutual consistency as the

distance from the burner mouth increases. This trend was discussed in connection to figure 16.

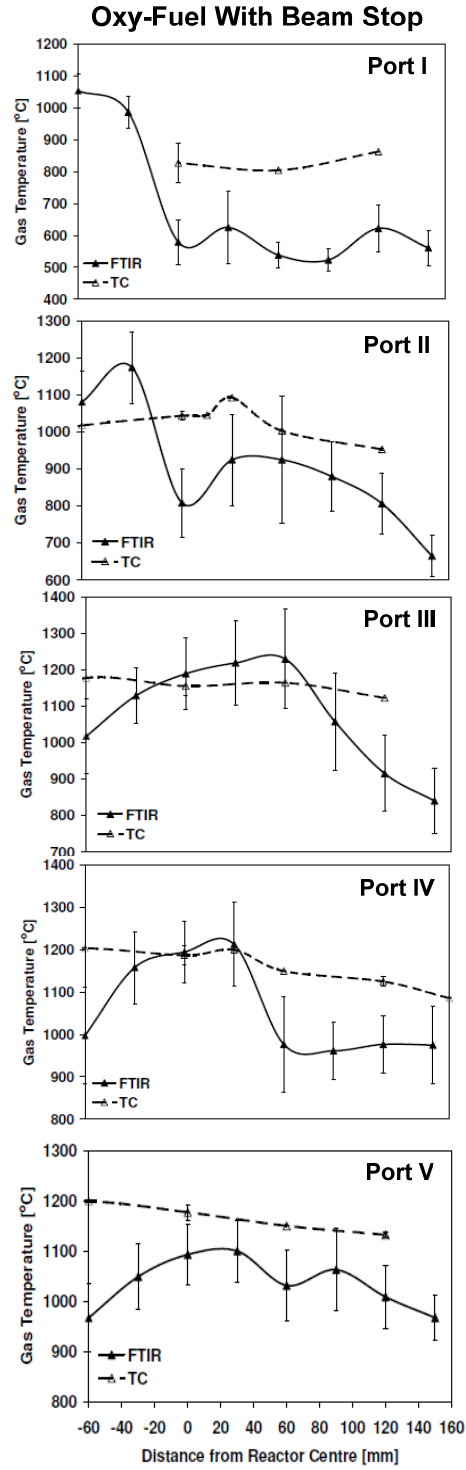


**Figure 17** Temperature profiles measured by the FTIR-probe and the S-type thermocouple during straw fired experiments.



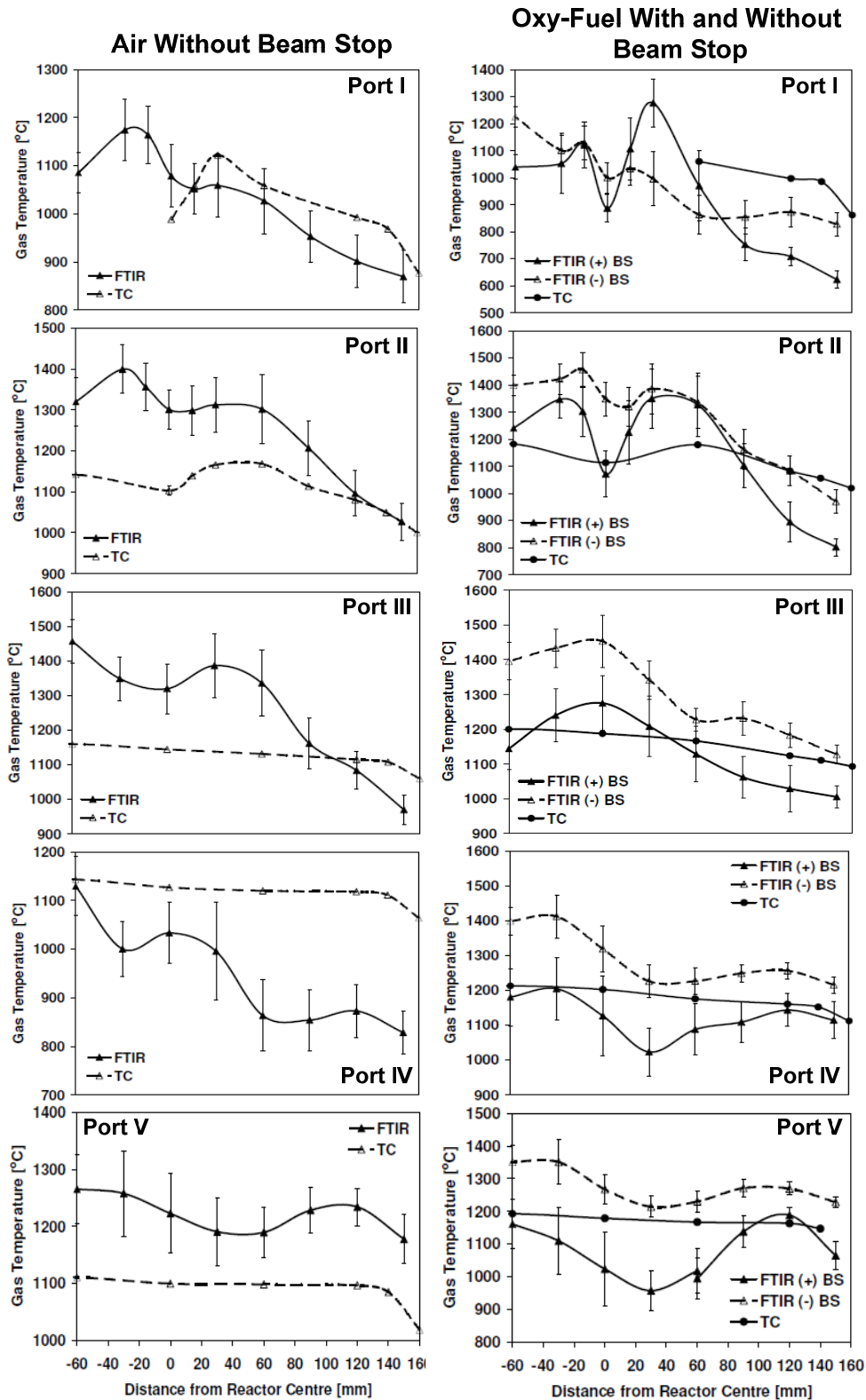


Figure 18 Temperature profiles measured by the FTIR-probe and the S-type thermocouple during experiments where a 50 wt. % mixture of coal and straw is used as fuel.

A comparison of gas temperature profiles between oxy-fuel and air combustion of a 50 wt. % mixture of coal and straw can be seen in figure 19. In general the temperatures are quite similar. This is expected as the oxy fuel conditions (30 vol.% O<sub>2</sub> in oxidizer, see Table 3) were determined to give similar temperatures [Toftegaard, 2011]. That an O<sub>2</sub> concentration of approximately 30 vol. % yields a temperature profile similar to air combustion is well documented in the literature [Toftegaard et al., 2010] and is due to the higher heat capacity of CO<sub>2</sub> being counterbalanced by a smaller overall flue gas volume and a higher reaction rate caused by the higher O<sub>2</sub> concentration. The temperature for air-blown combustion in port IV seems too low for reasons not known, and even increases again for port V.

## 2.6 Gas Phase Concentrations

The data time series of the gas phase concentrations are prone to fluctuations caused by the same sources (feeder instability, mixing limitation and general turbulent fluctuations) as discussed in connection to temperature measurements in figure 13 and figure 14 in section 2.5. As the tendency of fluctuations therefore is the same for concentration and temperature the subject will not be further dealt with in this section.

In the left-hand-side of figure 20, H<sub>2</sub>O profiles can be seen for combustion of straw, coal and the mixture of 50 wt. % straw and 50 wt. % coal. The right-hand-side of the figure shows CO<sub>2</sub> profiles for the same experiments. All of the profiles in figure 20 are found during combustion under oxy-fuel conditions as the absence of the beam stop during air firing makes interpretation of concentrations impossible (see section 2.4). From both the H<sub>2</sub>O and CO<sub>2</sub> profiles it can be seen that a high level of fluctuations (seen as the standard deviations in each data point) exists for measurements carried out through port I, especially at the reactor centre and especially when straw is used as fuel. That straw firing causes the largest standard deviations is related to the high volatile content, the influence of which was discussed in connection to figure 17. The reason for the significant fluctuations close to the flame is the same as for the temperature measurements, and relates to changes in the fuel feed rate, the flow structure and the degree of mixing (see sections 2.4 and 2.5).

**50 wt. % Straw & 50 wt. % Coal  
Measurements Without Beam Stop**

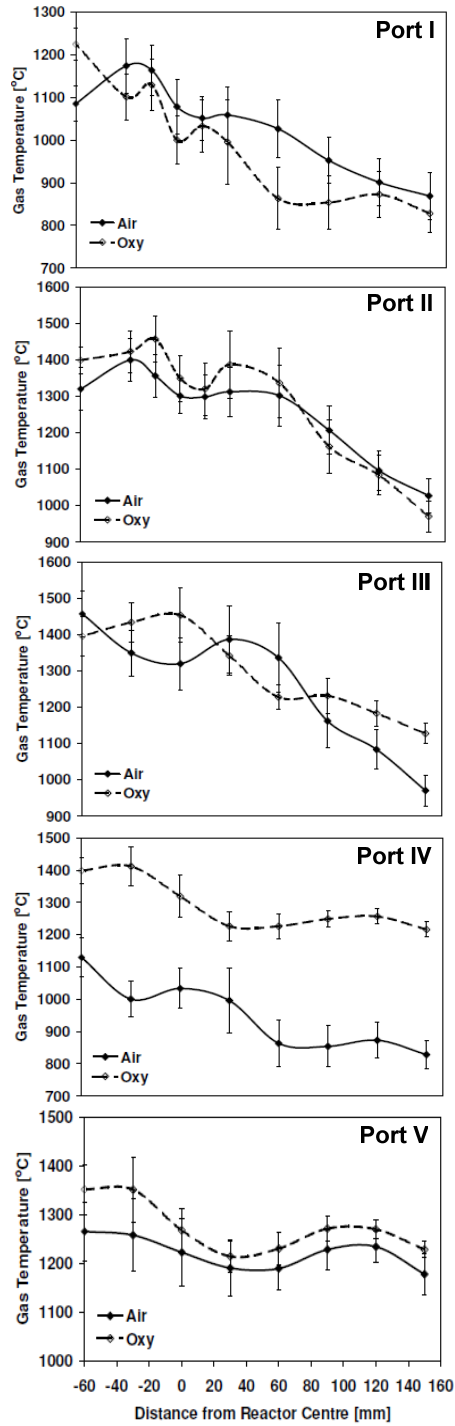
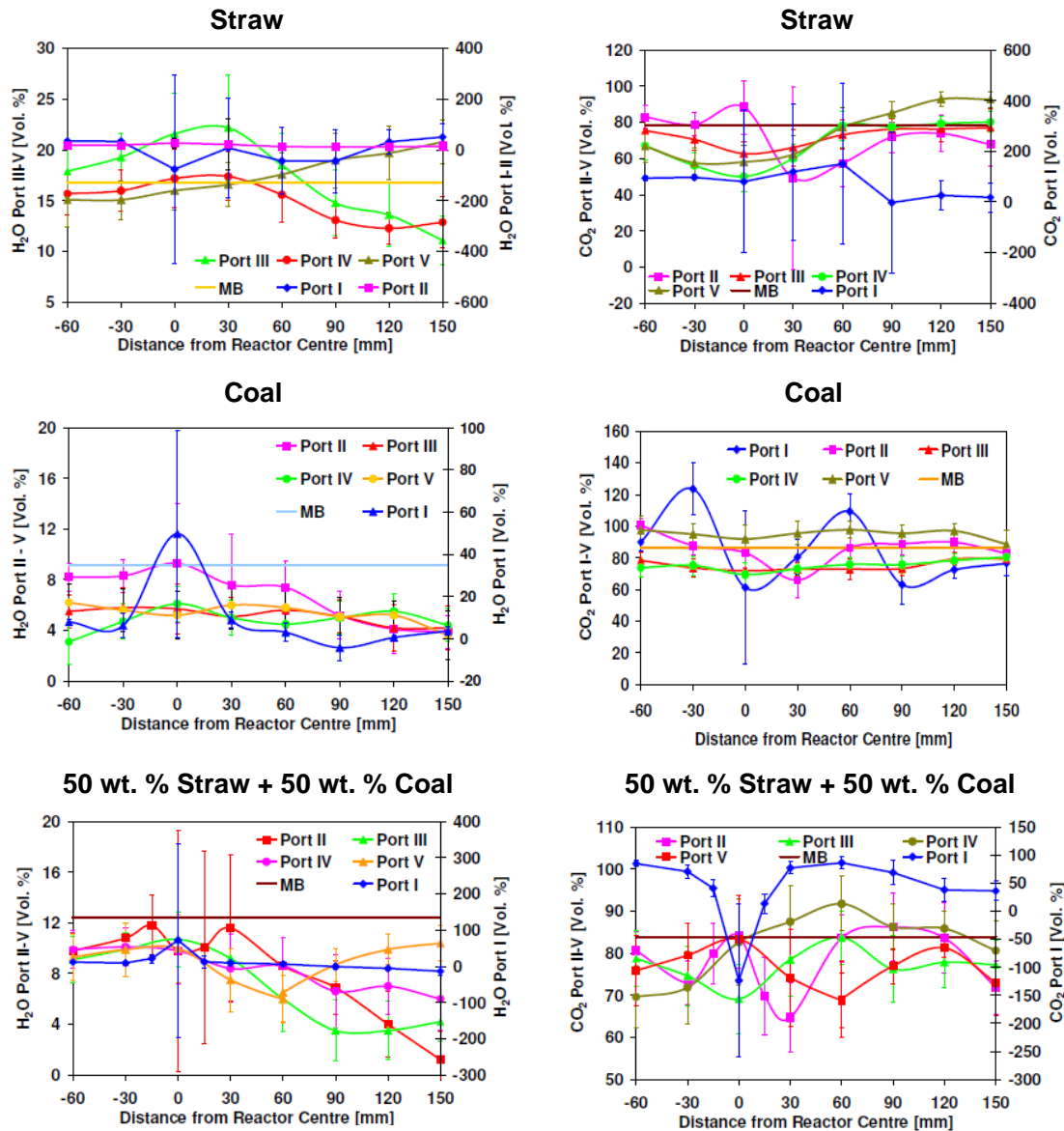


Figure 19 Comparison between the FTIR- and thermocouple temperature profiles in air and oxy-fuel experiments using both coal and a mixture of 50 wt. % coal and straw as fuel.

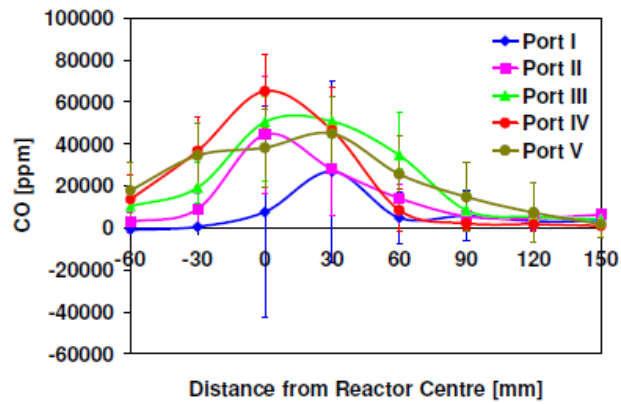


**Figure 20** Radial concentration profiles of  $\text{CO}_2$  and  $\text{H}_2\text{O}$  at the different measurement ports. All measurements are conducted during oxy-fuel firing with the beam stop in place in front of the ceramic tip. Also shown in the graphs are the calculated flue gas concentrations of the species corresponding to complete combustion and mixing (MB).

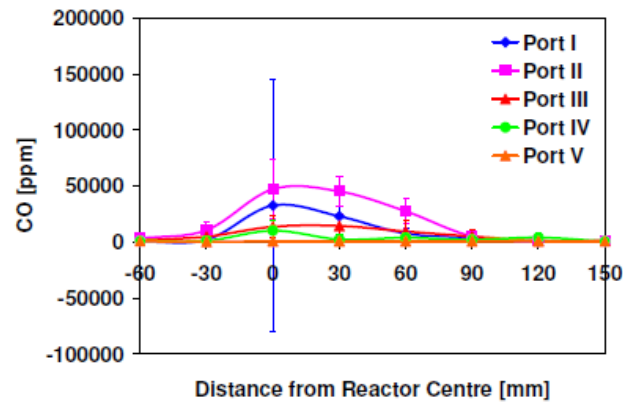
At the lower ports (III-V) the  $\text{H}_2\text{O}$  content measured using the FTIR-probe is in the same order as that found when the theoretical flue gas concentration is calculated from burner inlet data of fuel composition and gas flow assuming complete conversion and perfect mixing. This witness of a high degree of reliability of the FTIR-probe under conditions where the flow is well mixed, and where small scale flow structures do not disturb the

homogeneity of the optic path even though figure 20 show a general slight under prediction by the FTIR-measurements. This under prediction can however be influenced by differences in water content between proximate analysis and the fuel fired on the day of the experiments just as well as systematic inaccuracies caused by the high concentration of  $\text{H}_2\text{O}$  used as reference (see section 2.4) can play a role. The short optical path length can also cause lower concentrations as it will yield a weaker emission spectrum (see section 2.4). The  $\text{CO}_2$  profiles in figure 20 also witness of a good reliability of the FTIR-measurements as the measured profiles lie reasonably close to the theoretical concentrations of  $\text{CO}_2$  at the lower ports. From neither of the profiles in figure 20 it is possible to evaluate the flame structure as all of the profiles appear flat. In figure 21, that shows CO profiles from the same experiments as in figure 20, the flame structure and the degree of axis-symmetry are easier to evaluate. Large fluctuations in the concentrations (as evidenced by the standard deviations) were observed during a time series. The signal from CO is influenced by the same sources of uncertainty as  $\text{H}_2\text{O}$  and  $\text{CO}_2$  but being a reactive molecule makes the CO signal even more sensitive to differences in mixing, and especially to the local stoichiometry, in the optical path. The fluctuations again should be taken as a measure of the actual fast changing conditions in the reactor. The figure further illustrates the change in flame length and width with the change in fuel composition. Downstream of the flame the CO is typically very low due to sufficient  $\text{O}_2$  to oxidize CO to  $\text{CO}_2$ . However, near the flame front the concentration of CO can reach very high levels. For pure coal, the centreline concentration of CO (position 0 cm) drops to zero in port 5, whereas combustion of pure straw shows significant levels of CO (about 5% on average) at this distance from the burner. The flame length of pure straw is thus considerably larger than for pure coal due to the much larger particle size. This shows the importance of increased residence time on the burnout efficiency for increasing fuel straw share.

### Straw



### Coal



### 50 wt. % Straw + 50 wt. % Coal

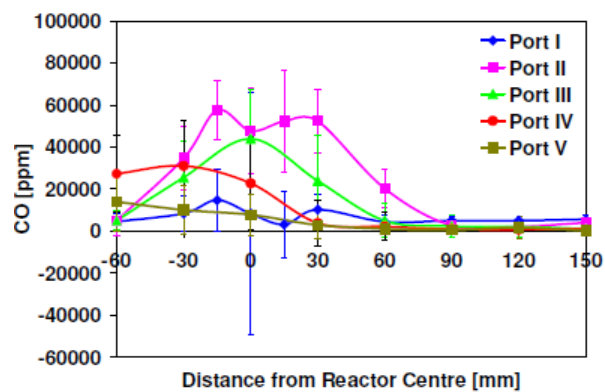


Figure 21 Radial concentration profiles of CO at the different measurements ports. All measurements are conducted during oxy-fuel firing with the beam stop in place in front of the ceramic tip.

### 3 Swirl Burner IR Measurements

#### 3.1 In-Flame Measurements by Thermal Imaging

A method for measurement of surface temperature and size of single fuel particles in laboratory flames by a fast and sensitive thermal IR (InfraRed) camera is described in the following. The technique is fast and easy to apply in laboratory flames where it can be used to map particle surface temperature, size and number density in selected positions of a flame through existing measurement ports where e.g. 1250 IR pictures are captured and statistics of 3000 - 23000 single particles obtained within one minute of measurement. The thermal pictures reveal local information about the combustion process and give a deeper insight into the physics of the flame. In the following sections the theory and principles of this method of flame measurement are outlined.

#### 3.2 Theory and principles

Radiation from soot is a factor that can cause large errors in particle temperature measurements. Absorption of soot varies with wavelength and is roughly 10 times larger in the visible region than in the mid infrared region of the light spectrum, which lowers the degree of disturbance during IR measurements. This is illustrated in figure 22.

As a strong absorber is also a strong emitter it might lead to large errors in measured particle temperatures when using a system (CCD camera) sensitive in the visible region of the light spectrum, as the temperature of soot particles can be significantly higher than that of large fuel particles. If a two-color pyrometric method were used for the measurements instead of the present, it would not improve results due to the same problems of radiation from soot. Therefore, a thermal mid-IR camera with a cooled InSb detector is used in the experiments. The InSb detector is sensitive in the wavelength range  $1.0 - 5.7 \mu\text{m}$  (in wavenumbers  $1754 - 10000 \text{ cm}^{-1}$ ), i.e. in a spectral region where  $\text{CO}$ ,  $\text{CO}_2$ ,  $\text{C}_x\text{H}_y$  and  $\text{H}_2\text{O}$  have emission bands. A typical emission spectrum for an oxy-fuel coal flame is shown in figure 23, where mainly  $\text{CO}_2$  bands at  $2350$  and  $3700 \text{ cm}^{-1}$  and a  $\text{H}_2\text{O}$  band at  $3800\text{-}4100 \text{ cm}^{-1}$  is seen. A  $3.9 \mu\text{m}$  ( $2564 \text{ cm}^{-1}$ ) optical interference filter, that is selective for this wavelength only, is inserted in front of the IR camera detector to avoid disturbances in particle temperature measurements from these gas bands.

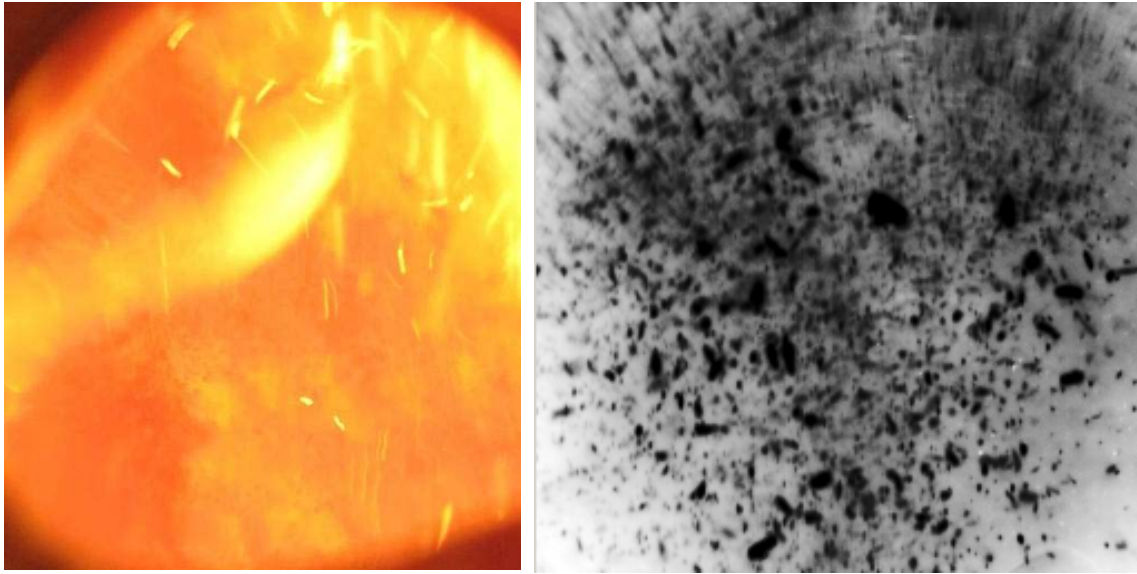


Figure 22 Left: Example of a picture of a flame taken with a digital camera. Tracks from hot particles are seen, but many particles are hidden by soot radiation. Right: Picture taken with an IR camera system. Here almost no effects are seen from soot. Particles appear dark as they are colder than the reactor wall in the background. Had they been hotter they would have been seen as bright spots.

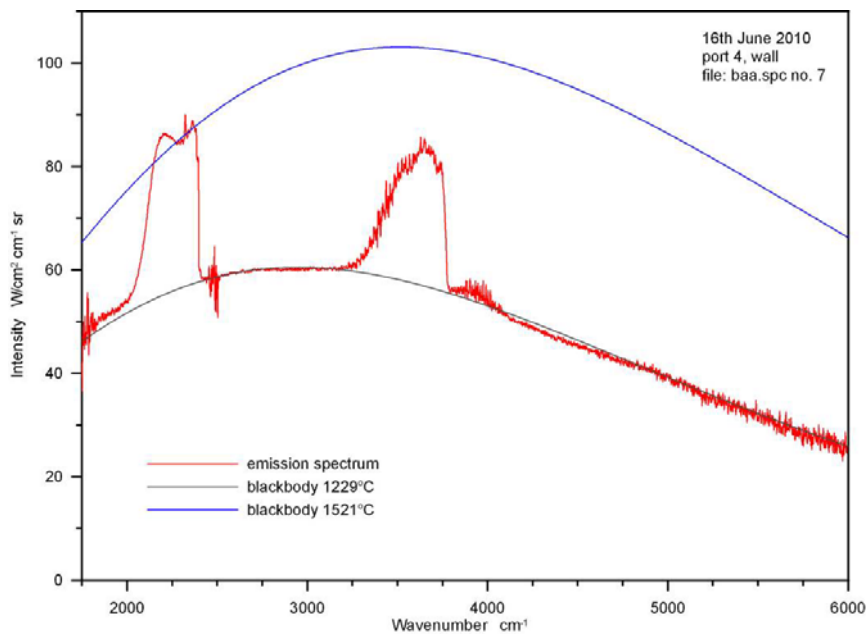
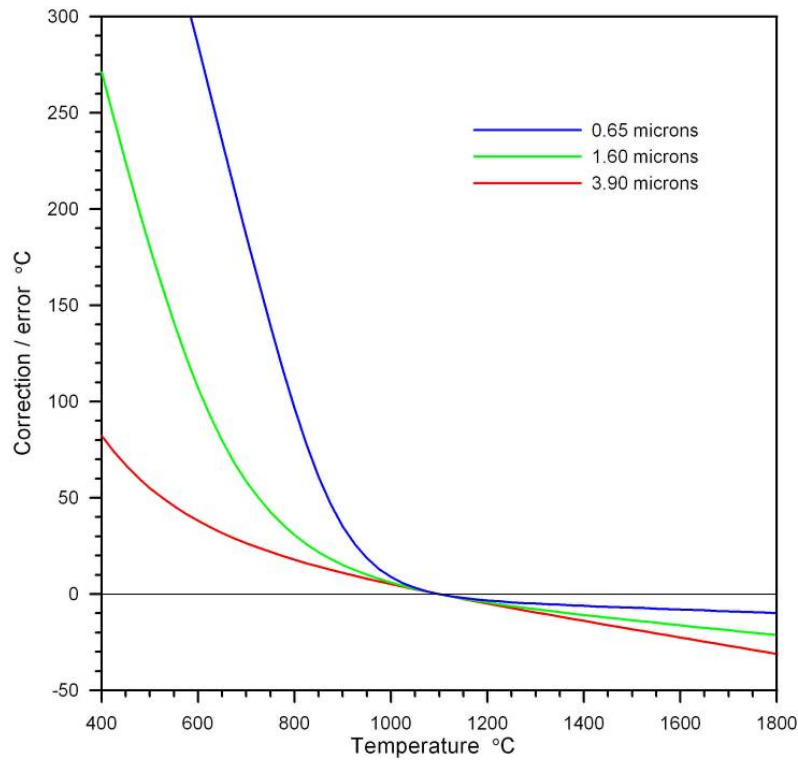


Figure 23 Snap-shot emission spectrum (red curve), measured during coal firing under oxy-fuel conditions with a FTIR spectrometer at port 4 (end of the flame), compared with blackbody curves at 1229°C and 1521°C. The gas temperature is approx. 1521°C as CO<sub>2</sub> emits like a blackbody around 2350 cm<sup>-1</sup>, but hot wing of CO<sub>2</sub> band at 2350 cm<sup>-1</sup> is equivalent to a gas temperature of 1560°C due to higher gas temperature inside reactor. Thermal emission from solid surfaces is mainly from the wall at the opposite side of the reactor and matches fairly well with a blackbody curve at 1229°C. X-axis is given in wavenumber cm<sup>-1</sup> (number of waves per cm). Range 1750 – 6000 cm<sup>-1</sup> which equals wavelengths between 1.67 – 5.71 μm.



Another important factor, when dealing with optical temperature measurements (those being two-color pyrometry, IR-measurements, or similar), is that measurement errors for particles colder than the surroundings increase when the wavelength decreases, as is seen in figure 24.

Planck's law (see eq. 4) can be used to calculate the influence of wavelength and emissivity of the particles for a given setup, see figure 25 as an example. The measured signal from a particle in a setup, such as that in figure 25, at a given wavelength  $\lambda$ , is given by eq. 2 where  $c$  is a calibration constant,  $\Omega$  the solid view angle,  $A$ , the detector area,  $L(\lambda, T)$  the Planckian equation (eq. 4) for a surface emitting like a blackbody and  $\rho$  the reflected light. In this scheme thermal radiation from soot and other particles is neglected, i.e. we look at a laboratory scale flame with good optical penetration of light.



**Figure 24** Errors on particle temperature measured at three wavelengths with a 5 % error on emissivity (i.e. a lower signal from the particle caused by e.g. a wrong emissivity) for a particle surrounded by walls at  $T_w = 1100^\circ\text{C}$ .

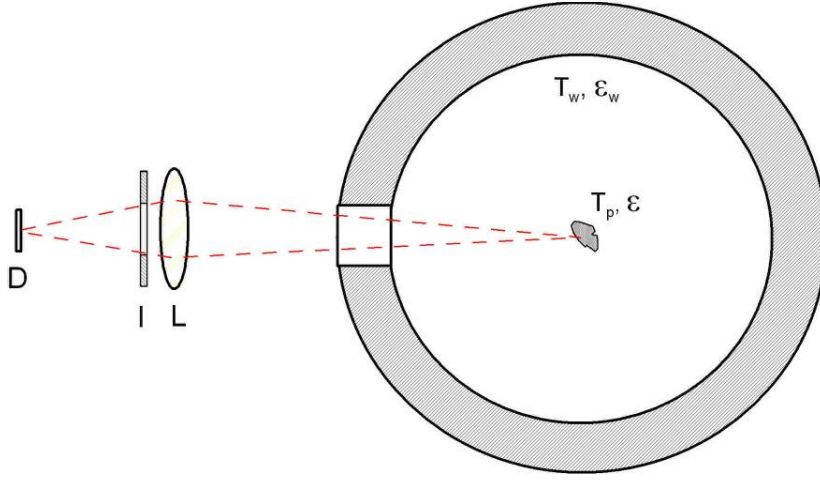


**Figure 25** Measurement situation with fuel particle at  $T_p$  and emissivity  $\varepsilon$  surrounded by hot reactor wall at  $T_w$  and emissivity  $\varepsilon_w$ . Viewing solid angle of detector D is defined by aperture I and lens L.

$$s = c \Omega A (\varepsilon L(\lambda, T_p) + \rho L(\lambda, T_w)) = c \Omega A (\varepsilon L(\lambda, T_p) + (1 - \varepsilon) L(\lambda, T_w)), \quad \text{Eq. 2}$$

The emissivity of reactor the wall,  $\varepsilon_w$ , has no influence on the result as the reactor can be seen as an enclosure with multiple reflections, i.e. like a blackbody cavity. This feature is important to pay notice to as it is fundamental for the particle temperature estimation. Eq. 2 can be used to correct measured brightness temperature of the particle for emissivity of the particle or estimate errors on the temperature measurement as illustrated in figure 24.

In the special case where the particle temperature equals the wall temperature the measured signal is described by eq. 3 and the particle becomes invisible in the thermal image or to the human eye no matter the emissivity of the particle, i.e. from the theory it is impossible to detect a particle using a passive method.

$$s = c \Omega A L(\lambda, T_w), \quad \text{Eq. 3}$$

A simple trick to detect particles under conditions where eq. 3 is fulfilled would be to have an optical port or cooled absorbing disk at the opposite side of the measurement port. This would mean that the particle becomes visible again due to a different background radiation temperature.

All particle temperature results in the following are given for a particle with emissivity of 1 (the brightness temperature). The emissivity correction is small according to figure 24, i.e. for a particle emissivity of 0.95 and a reactor wall temperature of 1100°C the temperature correction is +11.1°C at 900°C and -9.4°C at 1300°C. As the particles in the reactor are many hundreds degrees, having temperatures not far from that of the wall, the fractional error in the present procedure is therefore very small.

Most methods for particle temperature measurements are based on thermal light emitted from the surface of the particle. Radiation intensity as a function of temperature and wavelength is given by Planck's law in eq. 4 where  $C_1$  is the first radiation constant,  $C_2$  is the second radiation constant ( $C_1=0.5955 \cdot 10^{-16} \text{ W m}^{-2}$ ,  $C_2=0.014388 \text{ m K}$ ),  $\lambda$  is the wavelength and  $T$  the surface temperature in Kelvin.

$$L(\lambda, T) = \frac{C_1}{\lambda^5 (e^{\frac{C_2}{\lambda T}} - 1)} \quad \text{Eq. 4}$$

Planck's law can be used as a simple model to set up an equation to convert the measured radiation intensity to a surface temperature of a blackbody with an emissivity of 1 (brightness temperature) as shown in eq. 5.

$$\left. \begin{aligned} L(\lambda, T) &= \frac{C}{\lambda^5 (e^{\frac{C_2}{\lambda T}} - 1)} + L_0 \\ L' = L'(\lambda, T) &= L(\lambda, T) - L_0 \end{aligned} \right\} \quad T = \frac{C_2}{\lambda \ln(\frac{C}{L' \lambda^5} + 1)} \quad \text{Eq. 5}$$

In eq. 5,  $C$  is a calibration constant (gain factor) and  $L_0$  is an offset. The offset is mainly caused by thermal radiation from the IR camera itself, i.e. thermal radiation from the cameras inner parts before the optical band filter. A drift in camera temperature will affect the offset, but will only have a minor influence on the calibration factor  $C$  as the detector temperature in the IR camera is kept constant by a cooler. Figure 26 shows an example of the relation between radiation intensity and the temperature of the emitting source.

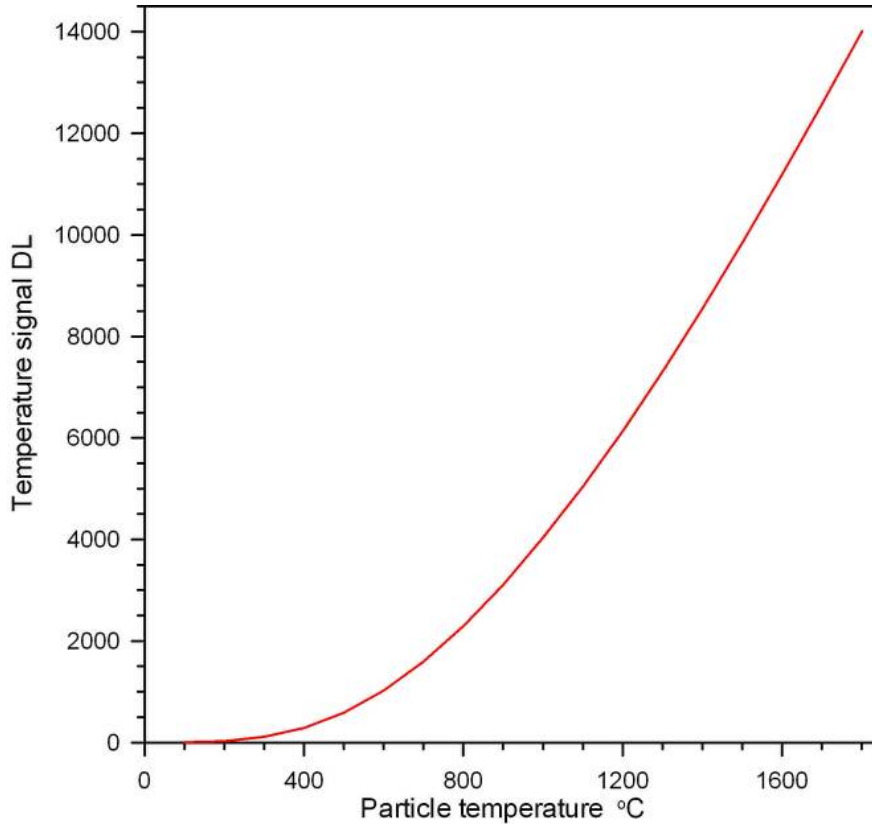


**Figure 26** Example of the signal-temperature relations from Planck's equation (eq. 5) at  $\lambda=3.9 \mu\text{m}$ . DL refers to digital level or signal measured at each pixel in the camera. A 14 bit signal is needed to cover a temperature range up to 1700 °C. The IR camera has 16 bit digital output, but works in practice with approx. 14 bit ( $2^{14}=16384$  levels).

### 3.3 Instrumentation

An IR camera of the type Cedip (now FLIR), model Titanium, with a Stirling-cooled InSb detector of 640 x 512 pixels and a maximal frame rate of 100 Hz was used in the experiments. The exposure time can be set from 7  $\mu\text{s}$  to 2300  $\mu\text{s}$ . The camera has a filter wheel with space for 4 filters in front of the detector and a 3.9  $\mu\text{m}$  optical band pass filter was mounted to avoid problems with emission or absorption effects from gasses. Special designed adaptor optics were needed due to a cold aperture placed inside the detector unit that would limit the field of view of the system with custom optics. The field of view of the system is defined by a single CaF<sub>2</sub> lens that is fixed to the IR camera. The effective area of the lens is reduced by an iris that reduces optical aberrations of the system and ensures a sharp image with small depth of field.

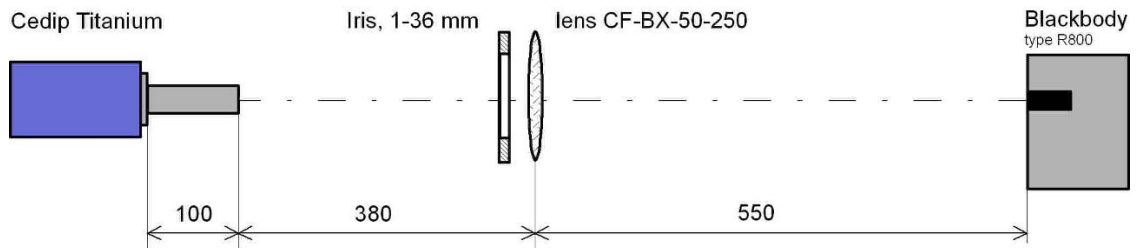


**Figure 27 Left:** Test setup with the IR camera, Cedip Titanium, used for particle temperature measurements. The IR camera is mounted with special designed adaptor optics that is 100 mm long. A  $\text{CaF}_2$  lens (ISP Optics CF-BX-50-250) with 250 mm focal length and image opening is positioned in front of a blackbody on array with the IR camera. The magnification is given by the lens formula, i.e. ratio of distance between lens and blackbody and distance between adaptor optics and lens.

The field depth of the system is only a few mm, i.e. particles located more than 5 mm outside the object plane is not seen or is just a shadow that can be filtered away by image processing. This means that measurements carried out at a specific radial reactor position is not influenced by the surroundings. The performance of the system was tested in a simple test setup, see figure 27.

The IR-system was calibrated before and after experiments with a portable blackbody source model R800 (Risø) with an uncertainty of  $\pm 3^\circ\text{C}$ . The system was mounted on the existing reactor ports with 4 screws, figure 28, and measurement planes adjusted in the range -60 mm to 150 mm (see figure 5)

### 3.4 Data analysis

The IR camera with optics was calibrated before experiments with a portable blackbody source at  $800^\circ\text{C}$  with 25 mm aperture and by looking at an object at room temperature (paper) to find the two calibration constants  $C$  and  $L_0$  (see eq. 5). The mean intensity in a circle of the two calibration pictures can be found using the standard thermal software “Altair” delivered with the IR camera, e.g.  $1792.5 \pm 10.4$  DL at  $800^\circ\text{C}$  and  $261.7 \pm 10.3$  DL at ambient temperature. A standard deviation of  $\pm 10$  DL corresponds to  $\pm 2^\circ\text{C}$  at  $800^\circ\text{C}$ , i.e. variations in pixel intensity is comparable to the uncertainty in the temperature of the blackbody calibrator.

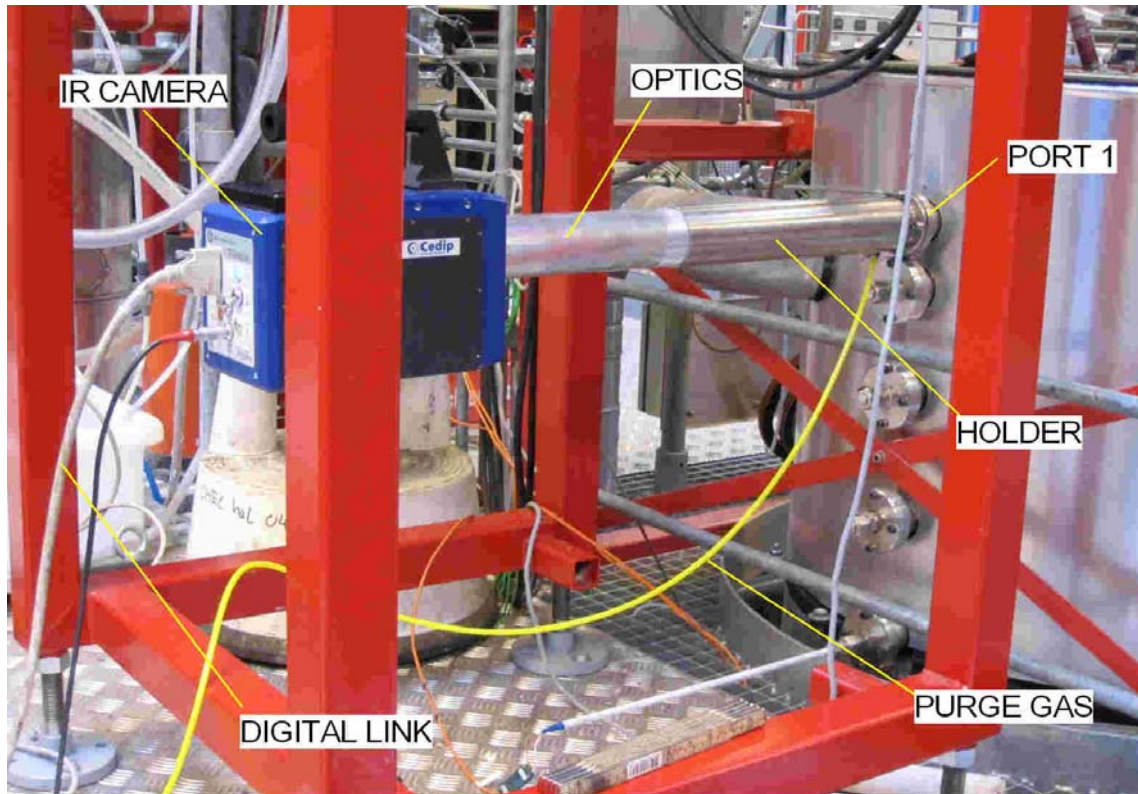


**Figure 28** IR-measurement of particle temperature and size at port 1. A holder is attached to port 1 with 4 screws. The holder carries the IR camera mounted with the special optics unit. The optics can be moved approx. 400 mm in the holder. Field of view in the flame can be adjusted from the wall of the reactor (at port 1) to 60 mm across the centre of the reactor.

Pictures were recorded and stored in raw digital format using the Altair software and the special “ptw” format for 16 bit multi files with a header containing all camera settings. Typical 1250 time tagged pictures were stored for each measurement position with a frame rate of approx. 30 Hz (within 41 s). The frame rate was reduced from 100 Hz by a factor 3 due to delays when storing images directly to disk compared to when storing images in the memory of the computer. Nevertheless, it was preferred to retrieve images recorded over a sufficiently long time to smooth out effects from the turbulent behavior of the flame. Lens exposure time was set to 17  $\mu\text{s}$  in the experiments, i.e. a particle with a velocity of 1 m/s move 17  $\mu\text{m}$  during recording of an image or approximately half the resolution of the camera (31.9  $\mu\text{m}$ ) in the object plane.

Thermal pictures in ptw format are analyzed after the experiments using a Labview application "PTWParticleDetectionAndRecording.exe". The number of particles is found and each particle is given a number in the picture and a mean intensity, minimum

intensity, maximum intensity, area in pixels, centre of mass/area (X,Y), elongation factor, bounding rectangular box, perimeter and ratio of equivalent ellipse axes is calculated. The user can control and follow the analysis of the pictures, e.g. set thresholds to avoid bias of statistics by particles not in focus, judge quality of pictures, etc. Data and settings in the analysis is stored in an Excel file for further analysis, i.e. intensities are converted to temperature in °C and dimensions converted to  $\mu\text{m}$  using calibration data. Particles with centre of mass outside the circle of focus:  $R^2 > ((X-319)^2 + (Y-255)^2)$  (red circle in figure 29) are neglected as data treatment of these particles is associated with a high degree of uncertainty.

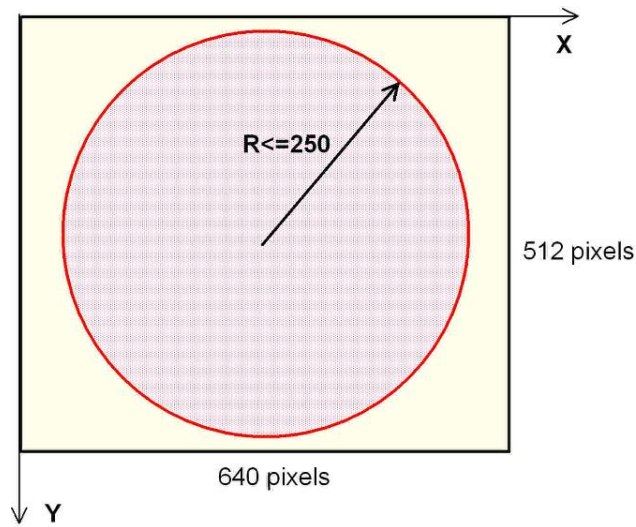


**Figure 29** Only particles with a centre of mass inside the red circle are accepted to avoid including particles at the border of the image and to mainly use the central part of sensor where the highest image quality and uniformity are found.

A basic problem in the present application is measurements on particles close to the reactor wall temperature as particles vanish and is not seen clearly in pictures (see section 3.2). The problem can be overcome if a cold background is introduced, e.g. a measurement port opposite the measurement port used, but this was not an option in the present work. Another challenge is to handle particles that are almost in focus and images with very high particles density. To overcome this problem images are filtered using image processing routines supported by Labview and a threshold has to be set to sort out defocused particles and particles with intensities close to that of the background.



### 3.5 Particle Temperatures and Size Distributions

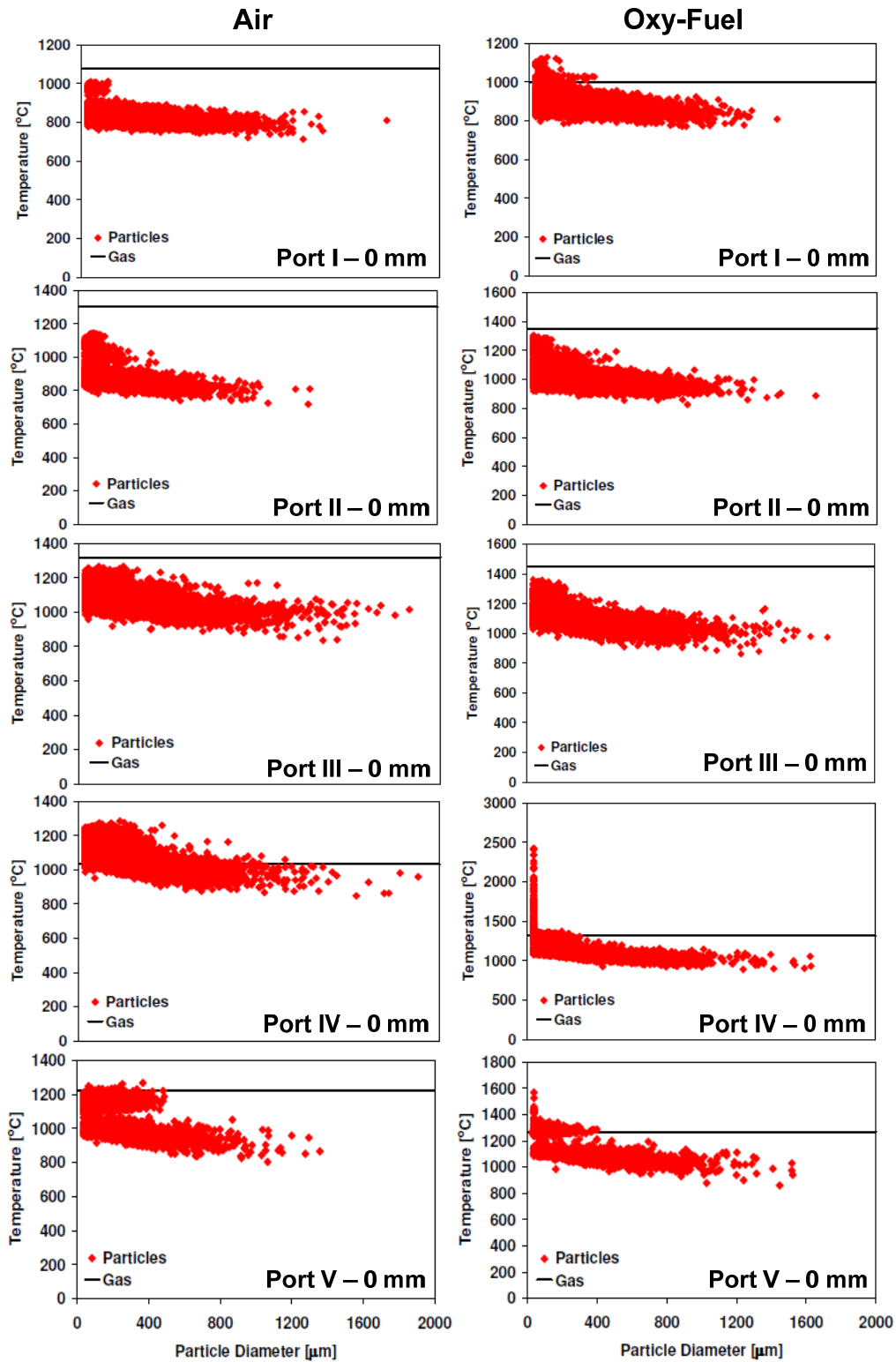
IR-measurements have been carried out in all the experiments listed in table 3, through all the five measurement ports and at 8-9 radial positions at each port and so the amount of data obtained is vast. The data obtained for coal firing is however not as accurate as that for straw firing. The reason for this is the large pixel size, which is suitable for identifying large straw particles in the images. When it is used to identify the much smaller coal particles (see figure 4) uncertainties do however arise when the large square sized pixels have to be used to estimate temperatures and equivalent circular radii's of the particles. For this reason the results of the coal fired experiments are not presented here. In the straw fired and coal/straw blend fired experiments the total amount of data is still too large to be presented in this report. As the main purpose of the measurements is to compare results between oxy-fuel firing and air firing the experiments with the coal/straw blend are chosen as representative. The reason for this is that both gas- and particle temperature measurements are available in all ports and all radial positions as FTIR measurements were carried out both with and without the beam stop during oxy-fuel firing. This means that comparison between oxy-fuel and air combustion can be made using both the gas- and particle temperatures.

Figure 30 and figure 31 show particle temperatures as a function of particle size at the reactor centre and near the reactor wall, respectively. Also shown in the figure is the gas phase temperature measured with the FTIR probe operated without the beam stop in place. It is seen that the particles in general burn at a higher temperature during oxy-fuel firing than during air firing<sup>1</sup>. This is due to the higher O<sub>2</sub> concentration (30 vol. % vs. 21 vol. % in air) that enables a faster heterogeneous reaction rate and hence a more intense particle heating. The gas temperatures in the two media are however fairly similar, which is better visualized in figure 19. In figure 30 it is seen that the particles at the reactor centre have temperatures lower than that of the gas phase, most clearly seen in the first three ports, whereas figure 31 show particle temperatures higher than that of the gas near the reactor wall.

---

<sup>1</sup> The very high particle temperatures seen in the figures for port IV and V for small particles in oxy-fuel combustion is caused by an erroneous pixel at a specific position in the picture. These temperatures are therefore not true but merely an indication of a instrumental/software imperfection encountered during the experiments.





**Figure 30** Particle temperatures measured at the reactor centre during oxy-fuel and air firing of a fuel mixture consisting of 50 wt. % and 50 wt. % coal. Also shown is the gas temperature measured using the FTIR-probe without beam stop.

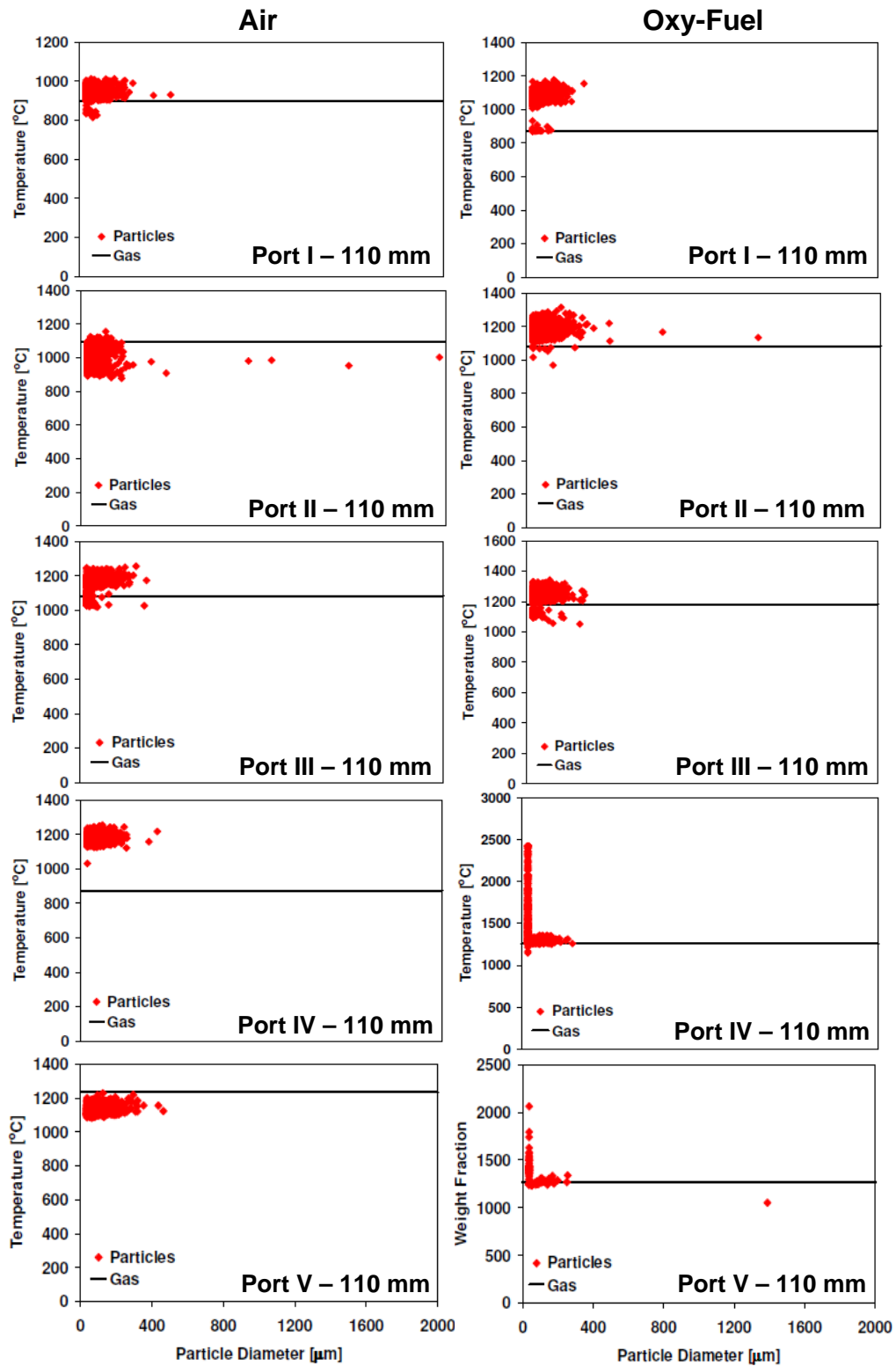


Figure 31 Particle temperatures measured near the reactor wall during oxy-fuel and air firing of a fuel mixture consisting of 50 wt. % and 50 wt. % coal. Also shown is the gas temperature measured using the FTIR-probe without beam stop.

In figure 30 it is seen that the difference in temperatures at the reactor centre between the gas and the particles during air firing is most significant at port II. During oxy-fuel firing the difference is most significant at port III. When figure 30 and figure 31 are compared it can be seen that the particle temperatures near the wall is only slightly higher than in the centre of the reactor. There is however a marked drop in gas temperature from the centre out to the wall at the first three ports. The full gas phase temperature profiles for the experiments using the mixture as fuel can be seen in figure 18, where the steep temperature gradient in, especially, the first three ports is seen clearly. As it was discussed in section 2.5 the part of the temperature profiles where the probe has crossed the burner mouth (negative radial values) are artificially high due to the effect of flame holding (see figure 3) and this part of the profiles in figure 18 is therefore not truly representative of the actual flame conditions. The temperature profile of the gas can be explained by the behavior of the devolatilization and the combustion of its gaseous products. Figure 32 shows a simplified schematic representation of the gas- and particle temperature profiles in the reactor. It can be seen that in the devolatilization zone, where gas phase reactions produce intense heat, a peak in the temperature profile will exist, marking a front between an oxidizing environment outside the flame and a reducing interior where the  $O_2$  concentration is lower due to consumption of volatiles. Around the peak in the gas temperature profile (including in this case the centre of the reactor) the gas phase temperature will be higher than that of the particles due to intense heating from homogeneous reactions and a lack of oxygen for heterogeneous reaction on the particles. At the first ports the endothermic processes of drying and devolatilization will also assist in keeping the particle temperature down. In figure 30 the delay in the temperature difference between gas and particles seen in oxy-fuel combustion compared to air-blown combustion is caused by the slower devolatilization and volatile ignition in oxy-fuel, a phenomena well documented in the literature [Toftegaard et al., 2010]. In connection to the preceding discussion it must be emphasized that the perfectly symmetric conditions indicated in figure 32 only serves as an illustrative example of the phenomena discussed. As discussed in sections 2.5 and 2.6 truly symmetrical conditions are not achieved in the experiments wherefore deviations in the trends of temperatures are seen in figure 18 and figure 30.

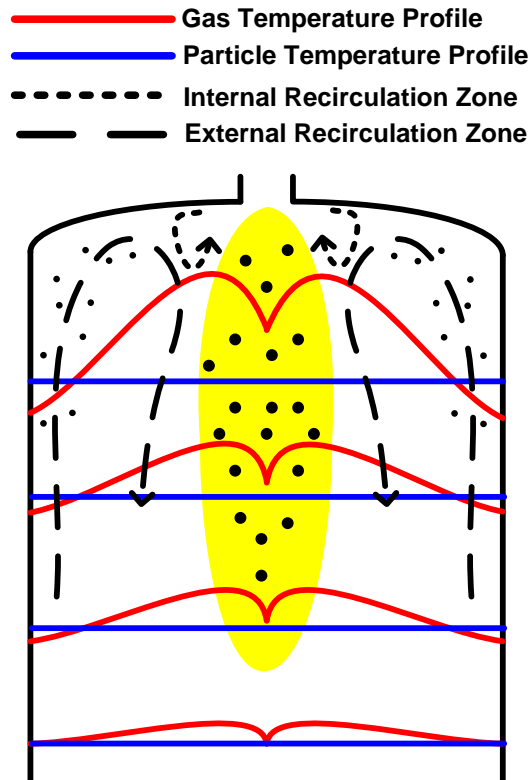
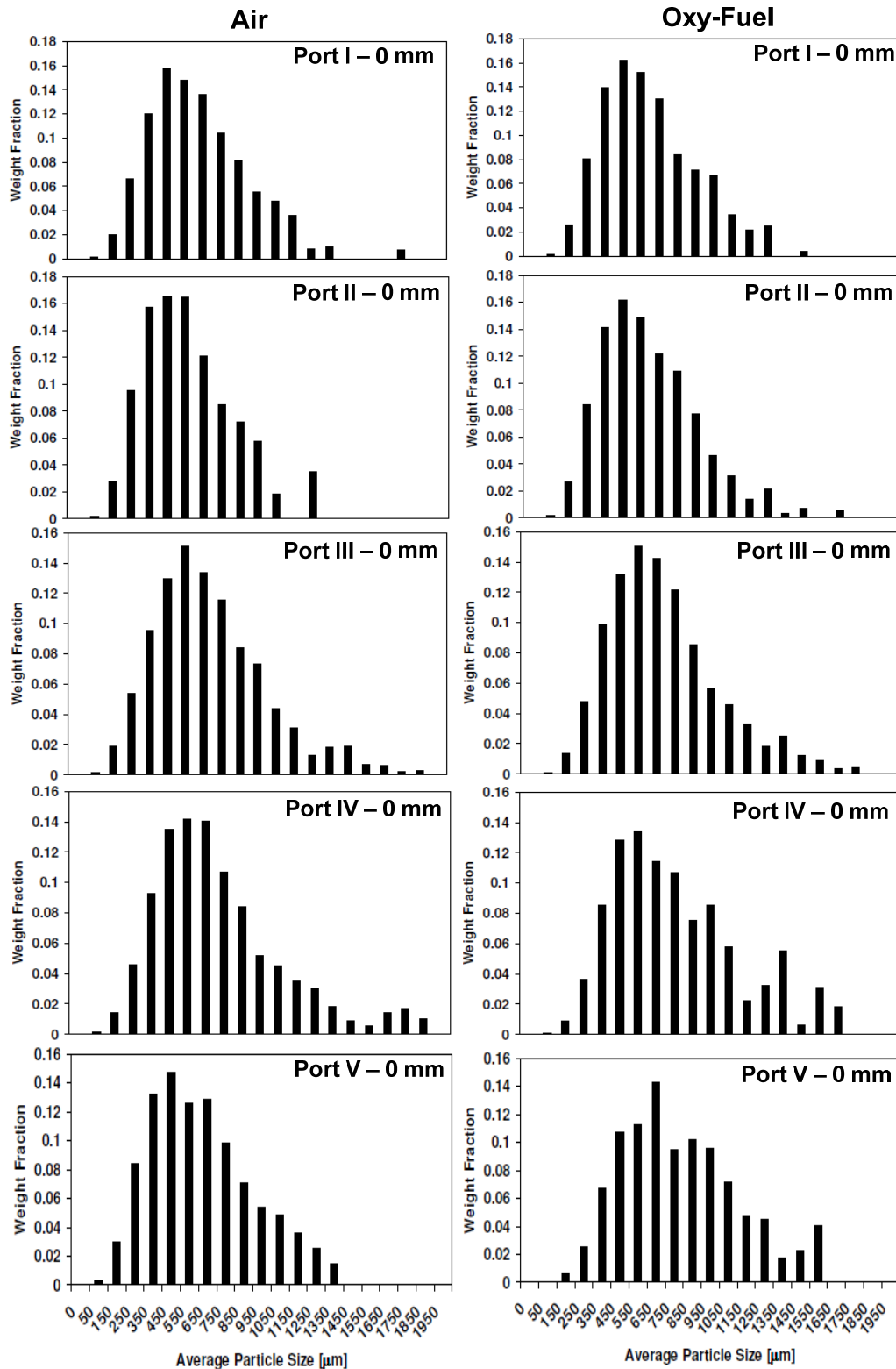


Figure 32 Simplified flow and temperature scheme of the swirl burner used in the experiments.

In figure 32 two different recirculation zones, an internal and external, are shown. The existence of the external recirculation zone is reflected in the discrete particle size distributions shown in figure 33 and figure 34. In these zones it can be seen that a broad particle size distribution is present at the centre of the reactor, reflecting that of the feed fuel, whereas the particle size distributions near the wall are narrow with smaller particles<sup>2</sup>. The small particles near the wall are carried upwards by drag forces by the external recirculation stream. The larger particles, having higher terminal velocities, are not carried upwards by the external recirculation drag.

<sup>2</sup>When it is stated that the particle size distributions in figure 33 and figure 34 are well defined as “broad” and “narrow” it is of course obvious that there are graphs that fall outside these definitions, especially in figure 34 where large particles are seen to make up the majority of the mass in some graphs. These “particles” are however not likely to be particles but instead unclear areas in the IR-pictures where dense particle clouds or optic phenomena are mistakenly taken as a particle by the data processing software. The definitions applied in the text are therefore representative of the actual fuel particles.



**Figure 33** Particle size distributions measured at the reactor centre during oxy-fuel and air firing of a fuel mixture consisting of 50 wt% straw and 50 wt% coal.

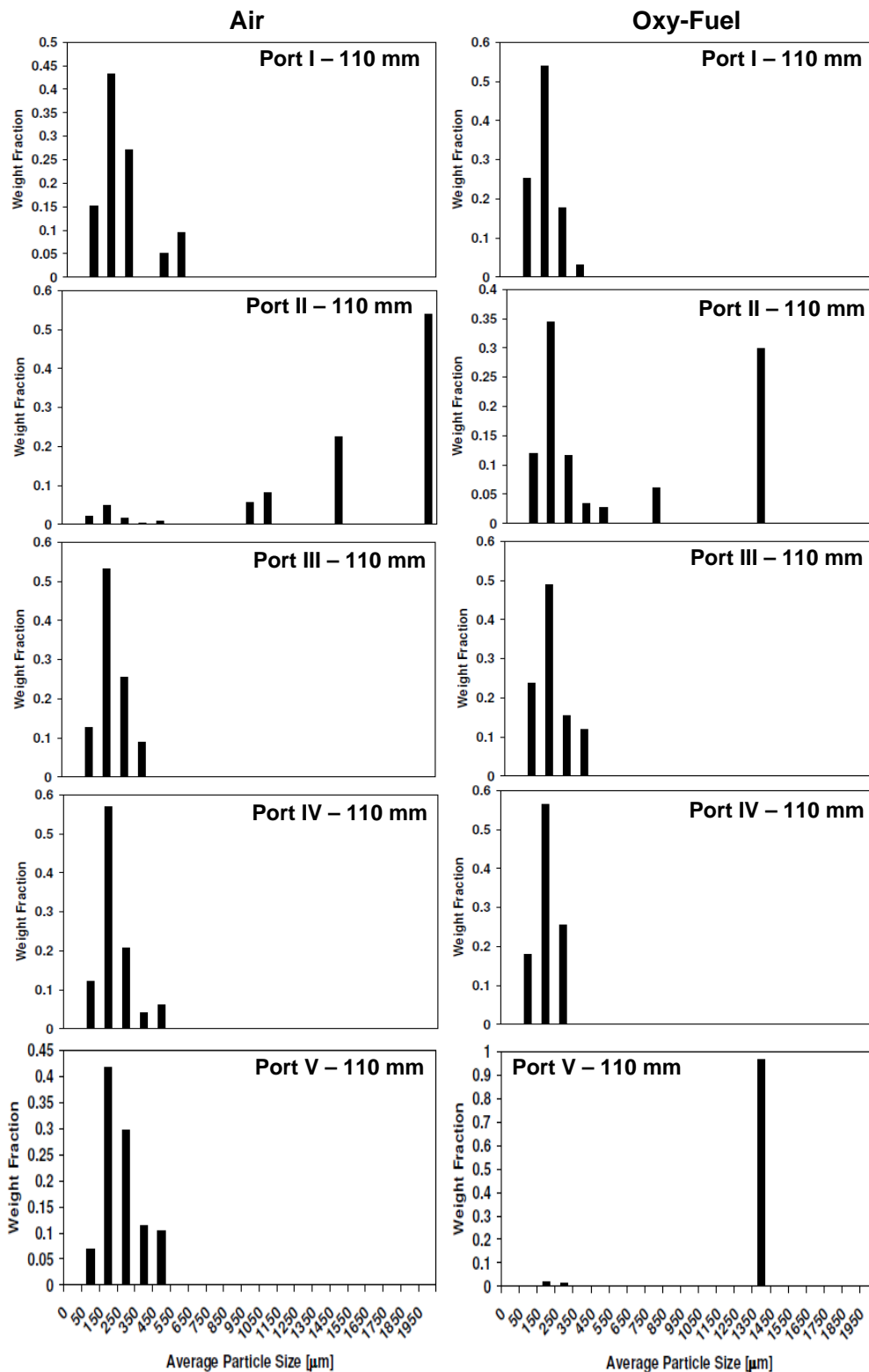


**Figure 34 Particle size distributions measured near the reactor wall during oxy-fuel and air firing of a fuel mixture consisting of 50 wt% straw and 50 wt% coal.**

## 4 The Fixed Bed Experiments

### 4.1 The experimental Setup

Experiments have been carried out in the laboratory scale fixed bed reactor shown schematically in figure 35. The reactor consists of an inner and outer quartz cylinder heated by three electrical heating elements. In all experiments the reactor was operated isothermally at 1073 K, showing fluctuations of less than 10 K through its centerline. The reactor inlet gas was preheated in the annulus between the inner and outer quartz cylinder before it flowed through the inner quartz cylinder where it made contact with the particle, cf. figure 35.

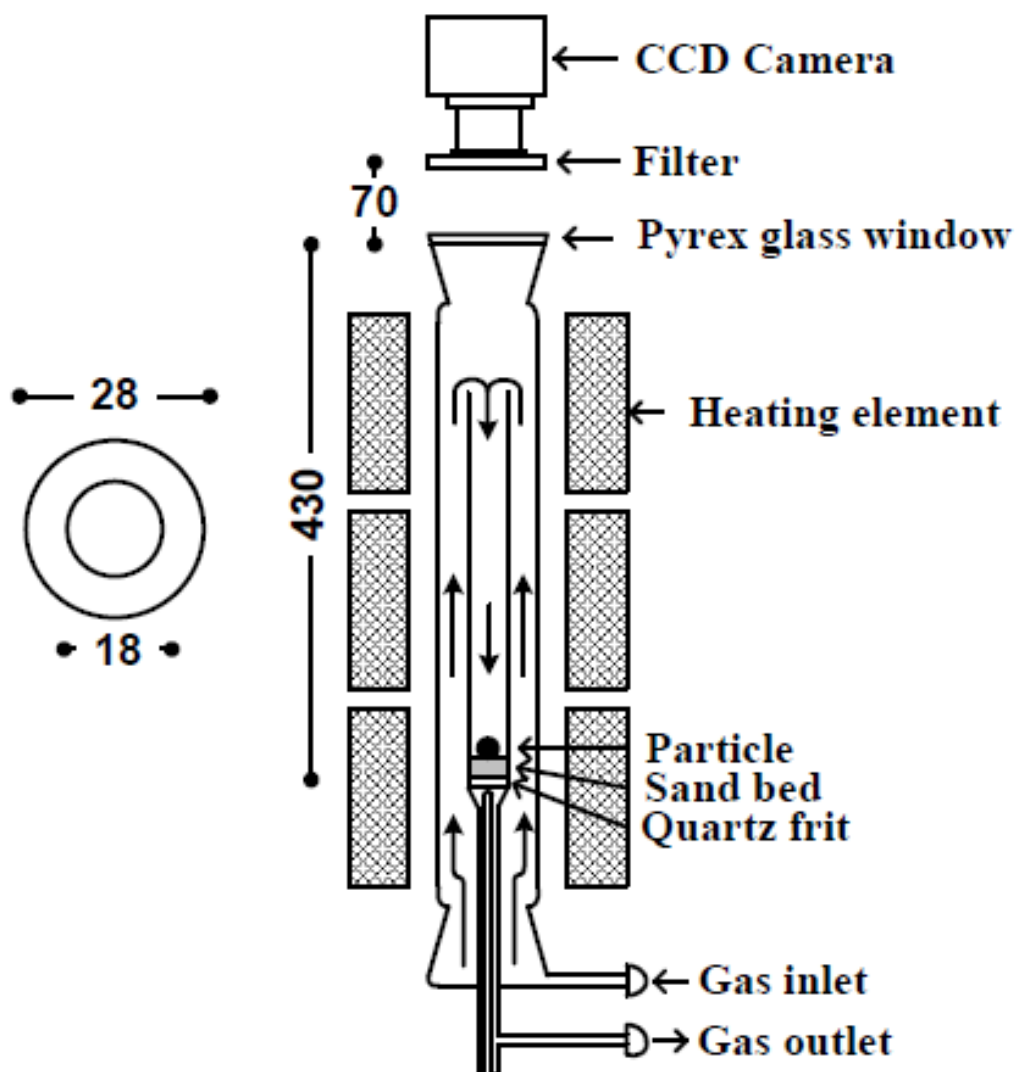


Figure 35 Experimental setup. Inlet gas is mixed from bottles. Length scale is in millimeters.

In all experiments the particle rested on a 5 mm bed of 300 - 355  $\mu\text{m}$  sand particles on top of a quartz frit to ensure its fixation during combustion and to protect the frit. Gaseous atmospheres were created by mixing bottled gases and the volumetric flow has been 1  $\text{Nl min}^{-1}$  in all experiments with  $\text{O}_2$  concentrations ranging between 5 and 80 vol. % in either  $\text{N}_2$  or  $\text{CO}_2$ . The majority of the experiments have been conducted with a single particle, weighing between 1.3 – 543 mg, but a series of experiments with 5, 10, 15 and 20 particles in both  $\text{O}_2/\text{N}_2$  and  $\text{O}_2/\text{CO}_2$  have also been carried out to investigate the effect of particle concentration.

A pyrex glass window was mounted on top of the reactor, directly above the bed, through which a 16 bit CCD camera measured the intensity of the Near Infra Red (NIR) radiation emitted by the particle. To ensure pure NIR measurements and to avoid saturation of the camera's light sensor, a filter was placed in front of the lens.

The NIR CCD camera used was a Stingray F033 from Allied Vision Technologies and had a 14 bit analog to digital converter, identical to the practically applied number of bits used by the camera in the swirl burner experiments. An extra 2 bit of unsigned resolution was however achieved here by averaging a series of shutter intervals thereby providing a total of  $2^{16} = 65536$  digital levels that could be detected by the camera. This is done on the expense of speed, meaning that it takes longer to take pictures in this setup than during experiments in the swirl burner. This will however not cause problems as the particle sizes and therefore time scale of the process are significantly increased here. The digital level is a measure of the photon radiation intensity. The maximum digital level corresponds to a saturation of the detector and its processing system and it therefore relates to the maximum measurable particle temperature, which is higher in this setup (necessary due to very high  $\text{O}_2$  concentrations) than in the swirl burner setup. A filter, that only allows radiation in the wavelength interval 710 – 1100 nm (NIR) to reach the sensor, was placed in front of the camera. The camera was calibrated with the filter in the temperature interval 1023 K – 1873 K using a black body source. This temperature interval was adequate for the experiments presented here. The filter served two purposes: It avoided saturation of the camera at each temperature and it reduced the influence of scatter caused by background radiation (from the reactor, the surrounding and the reactor



gas). The relationship between particle temperature and camera response was modeled by integration of Planck's law over the wavelength interval of the filter, similar to the calibration done for the camera in sections 3.2 - 3.4. Constants accounting for the emissivity of the radiating source, the transmittance of the filter and optics and the camera sensitivity were established during calibration. The sensitivity of the temperature measurements towards potential changes in source emissivity, e.g. ash layer formation during combustion, were tested and found negligible (changes were a few K). Data acquisition during the experiments was done using a LabVIEW program developed specifically for this setup and output were given both as movies made up from still images and data files.

It is important to emphasize that because the camera was recording the NIR radiation from the part of the particles surface that was positioned in its view point reported temperatures are surface temperatures of this area. Throughout the text the term "Maximum Particle Temperature" refers to the highest temperature measured during an experiment.

## **4.2 Fuels and Char Preparation**

Experiments have been conducted using chars from bituminous El Cerrejon coal and from German Lausitz lignite coal. Proximate and ultimate analyses of these coals are shown in table 4.

To prepare the chars, coals were dried at 378 K for app. 22 hours. Then the dry coals were sieved into the size intervals: 0.71 – 2 mm, 2 – 4 mm, 4 – 7 mm and 7 < mm. A size fraction of 1.7 – 2.36 mm bituminous coal particles was also prepared and used for experiments with several particles present in the reactor. Each of the size fractions were pyrolysed at 1173 K for 2 hours in N<sub>2</sub> to ensure that volatiles would not interfere with gas analysis during the experiments. During the pyrolysis no swelling was observed wherefore the size intervals remained intact. Pyrolysis was also carried out using CO<sub>2</sub> at the same conditions. The resulting chars have not been used for combustion experiments, however, as gasification caused additional weight losses of 8 – 20 wt. % for bituminous coal and total conversion of the lignite coal.

**Table 4 Proximate and ultimate analysis of the coals used in this study.**

	<b>El Cerrejón (bit.)</b>	<b>Lausitz (Lign.)</b>
<b>Proximate Analysis</b>		
LHV [MJ/kg]	24.70	20.43
Moisture [wt. % wet]	12.20	10.21
Volatiles [wt. % wet]	31.00	28.25*
Ash [wt. % wet]	11.30	4.85
<b>Ultimate Analysis</b>		
C [wt. % dry]	70.62	64.32
H [wt. % dry]	4.78	5.44
O [wt. % dry]	9.32	23.37
N [wt. % dry]	1.59	0.63
S [wt. % dry]	0.80	0.82

\*Calculated from muffle furnace pyrolysis at 1173 K in N<sub>2</sub>.

### **4.3 Particle Temperatures and Burnout Times**

For each of the experiments conducted in this investigation a dynamic particle temperature profile has been obtained. Figure 36 shows an example of these profiles for combustion of 2 – 4 mm bituminous char particles at 20 vol. % O<sub>2</sub>.

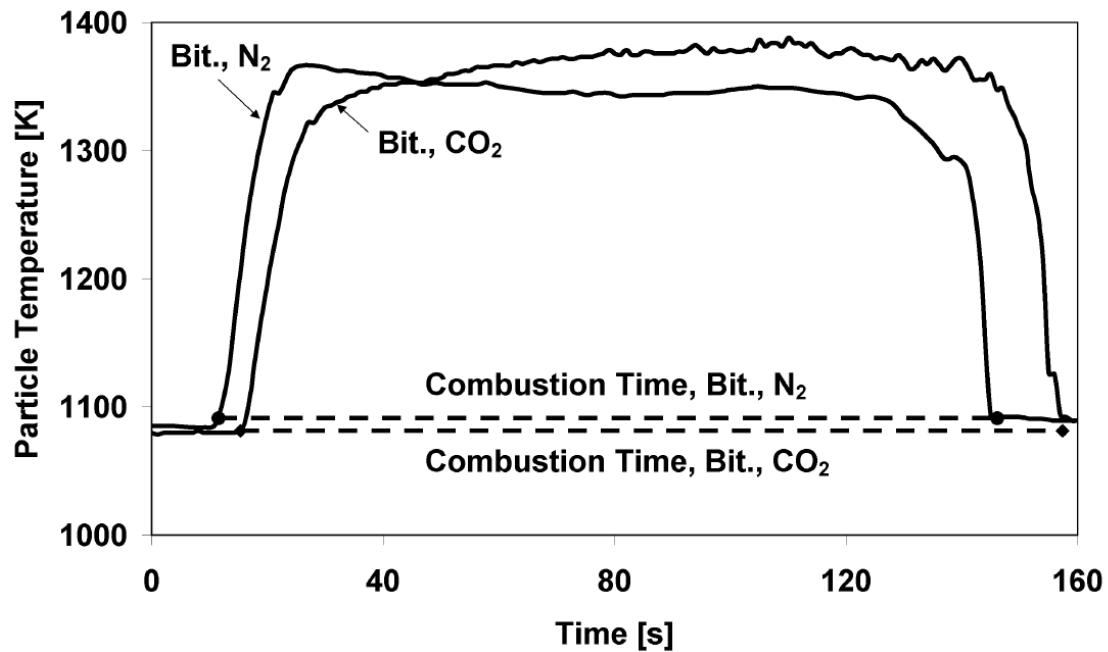


Figure 36 Particle temperature profiles from single particle combustion of bituminous char at 20 vol. %  $O_2$  in  $N_2$  and  $CO_2$ .  $d_p = 2 - 4$  mm.  $T_{\text{reactor}} = 1073$  K.

In figure 36 the dashed lines indicate the combustion times of the particles used in the experiments. For all experiments presented in this text a combustion time has been estimated this way, using the transient behavior of the temperature profile. The ability to use the temperature profiles to evaluate combustion times is a strong advantage of the IR-technique as the very high  $CO_2$  concentration during oxy-fuel combustion means that a combustion time cannot be found from the  $CO_2$  signal from the gas analyzer.

The temperature profiles in figure 37, which shows the effect of  $O_2$  concentration, show that higher particle temperatures are reached for bituminous char than for lignite char, but that both types of particles reach significant over temperatures. The reason for the difference between the two types of char is not clear, and somewhat counter-intuitive as the lignite is significantly more reactive than the bituminous coal char. Further experiments would be needed to clarify this.

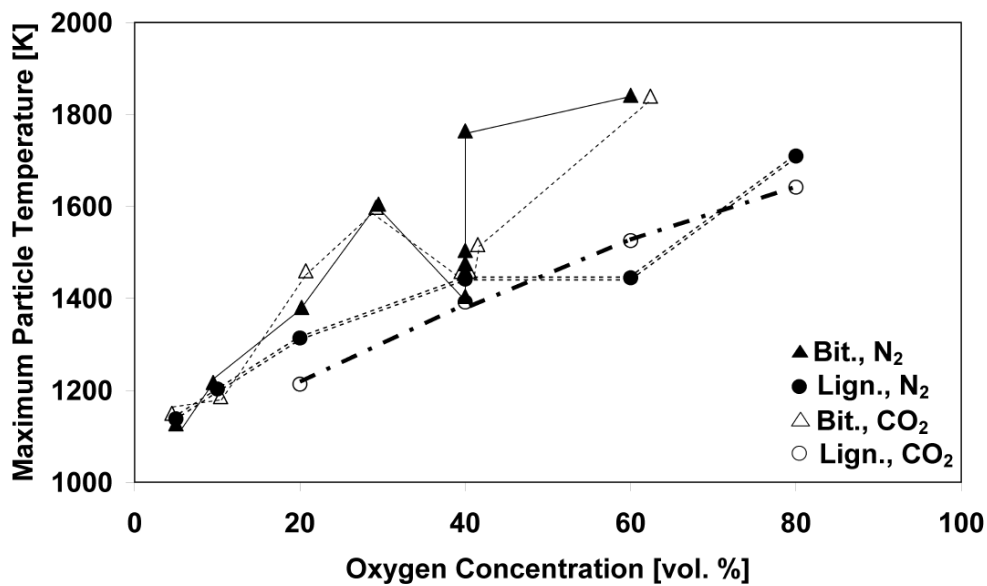


Figure 37 Maximum particle temperatures achieved during single particle combustion as a function of O<sub>2</sub> concentration.  $d_p = 2 - 4$  mm.  $T_{\text{reactor}} = 1073$  K.

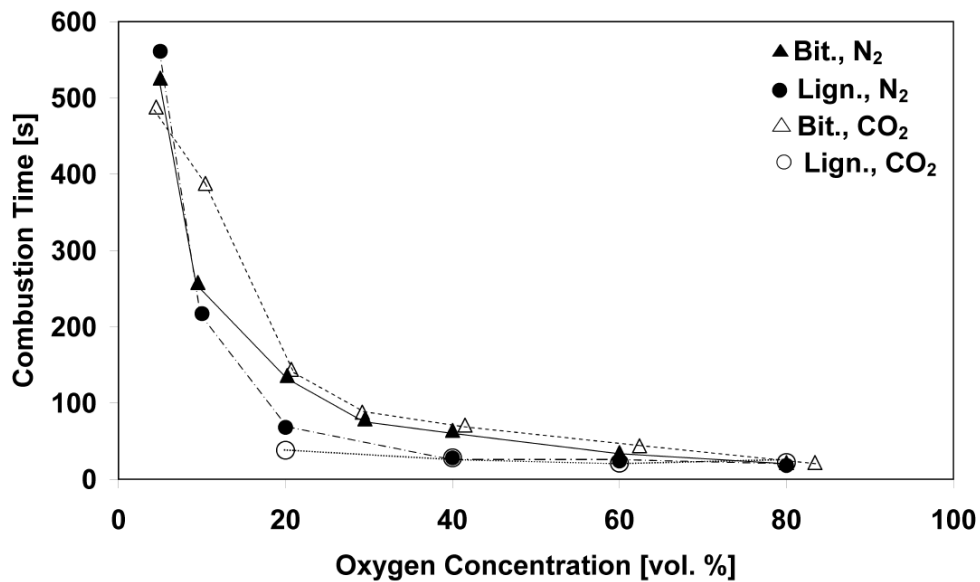
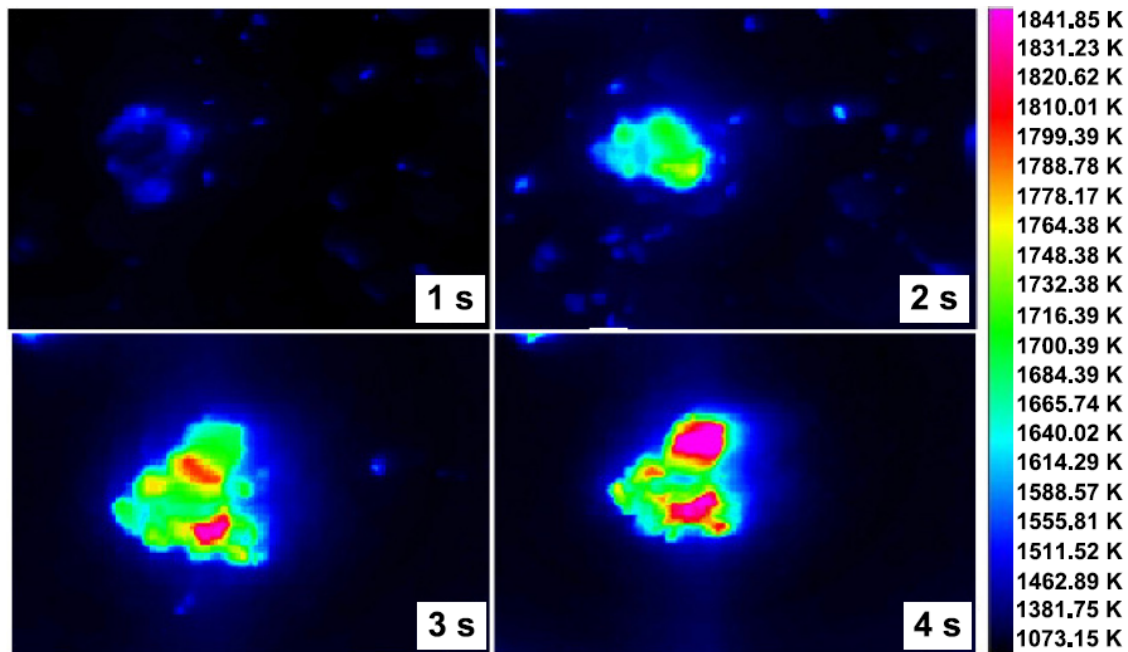


Figure 38 Burnout times for single particle combustion as a function of O<sub>2</sub> concentration.  $d_p = 2 - 4$  mm.  $T_{\text{reactor}} = 1073$  K.



**Figure 39** Still images of a single bituminous particle burning at 80 vol. % O<sub>2</sub> in N<sub>2</sub>.  $d_p = 3.5$  mm.  $T_{\text{reactor}} = 1073$  K. Time zero is ignition.

Figure 39 shows still images of a 3.5 mm bituminous char particle burning in 80 vol. % O<sub>2</sub> in N<sub>2</sub>. It can be seen that glowing fragments appear on the sand bed the first seconds after ignition. This was seen for all the experiments carried out with bituminous char in 60 or 80 vol. % O<sub>2</sub> in both N<sub>2</sub> and CO<sub>2</sub> and it is believed to be caused by the rapid release of gases during a secondary devolatilization that is brought upon by a fierce heating. The heating itself may also contribute to the fragmentation as thermal tensions will develop in the fragile char structure. A similar behavior was not observed for lignite char. Figure 39 witness of the strength that visual recording of a combustion process has when structural modeling is to be attempted, as evidence for this kind of explosive behavior could not have been documented without the NIR CCD camera.

In figure 40, that shows the effect of particle concentration, it is seen that the temperature of the hottest particle on the bed increases up to 150 K when the particle concentration increases from 5 to 20, though the increase is most pronounced for combustion in N<sub>2</sub>. The increase in particle temperature, caused by an increased heat of reaction mutually exchanged between the particles, sand bed and gas, is steepest for combustion in N<sub>2</sub>. This is due to the higher specific heat capacity of CO<sub>2</sub>, that is known also to influence ignition

behavior and temperature profiles in pulverized combustion [Liu et al., 2005], [Molina & Shaddix, 2007], limitations in burning rate caused by the lower O<sub>2</sub> diffusion coefficient in CO<sub>2</sub> [Brix et al., 2010] and possibly by increased absorption of particle radiation in CO<sub>2</sub>.

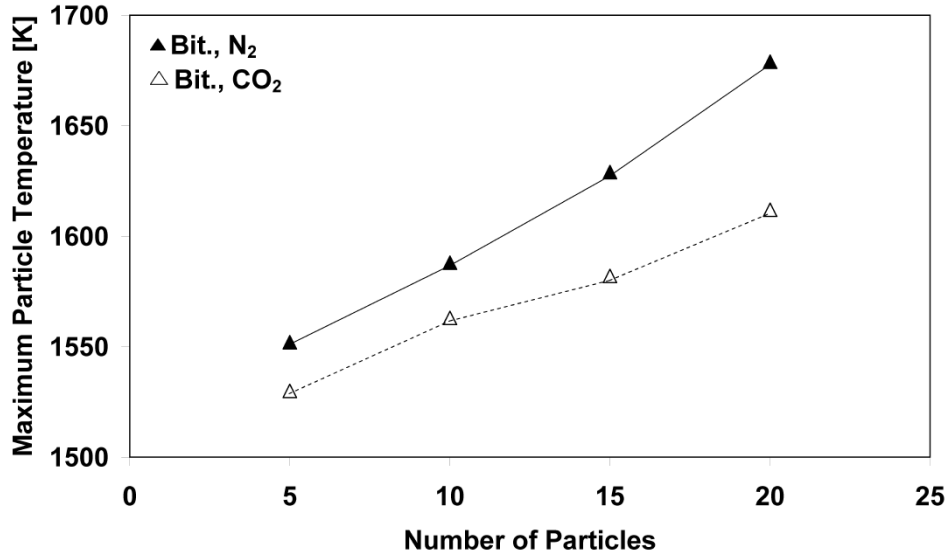


**Figure 40** Maximum particle temperatures of the hottest particle achieved during combustion of multiple particles at 30 vol. %.  $d_p = 1.7 - 2.36$  mm.  $T_{\text{reactor}} = 1073$  K.

In figure 41, that shows the effect of particle mass for a single particle burning in 40 vol.% O<sub>2</sub>, the particle temperatures increase initially with particle mass until approximately 0.01 g after which the profiles flatten (for bituminous char in O<sub>2</sub>/N<sub>2</sub> there is an outlier that breaks this trend). There is no consistent difference to be found between temperatures of bituminous char whereas the temperature of lignite char is consistently lower in O<sub>2</sub>/CO<sub>2</sub>. In figure 42 particle temperatures for bituminous coal char burning in 30 vol.% O<sub>2</sub> are fluctuating around a constant value irrespective of particle mass with a trend of lower temperatures in O<sub>2</sub>/CO<sub>2</sub>.

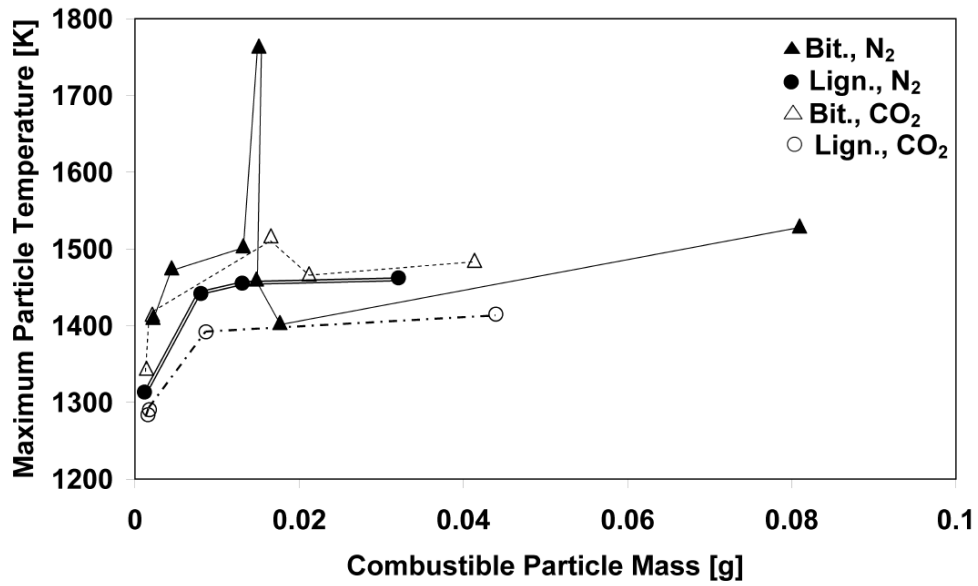


Figure 41 Maximum particle temperatures achieved during single particle combustion at 40 vol. % O<sub>2</sub> as a function of particle mass.  $d_p = 0.71 - 7$  mm.  $T_{\text{reactor}} = 1073$  K.

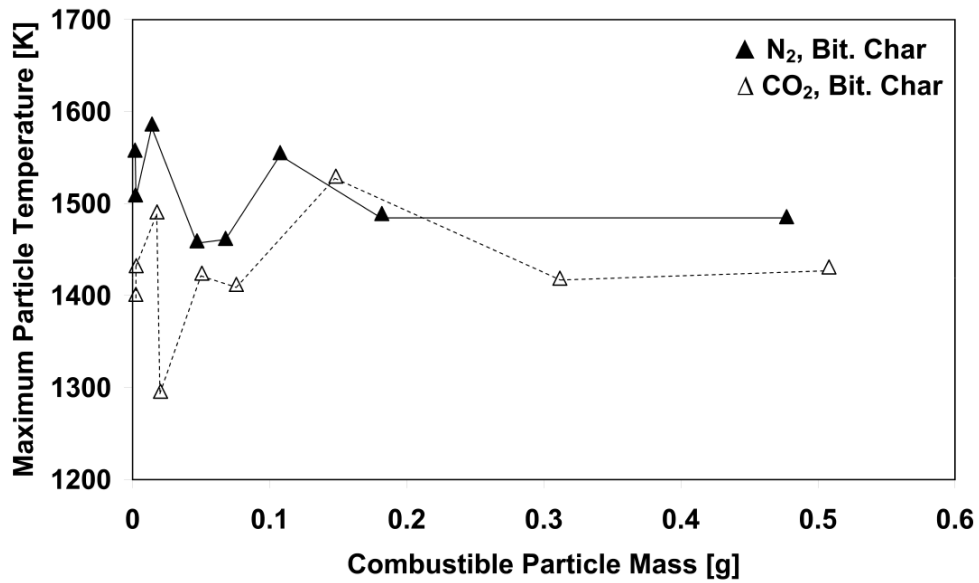


Figure 42 Maximum particle temperatures achieved during single particle combustion at 30 vol. % O<sub>2</sub> as a function of particle mass.  $d_p = 1.3 - 12.1$  mm.  $T_{\text{reactor}} = 1073$  K.

In figure 43 and figure 44 burnout times, found in the experiments from figure 41 and figure 42, can be seen to increase rapidly for both lignite char and bituminous char as the particle size increase.

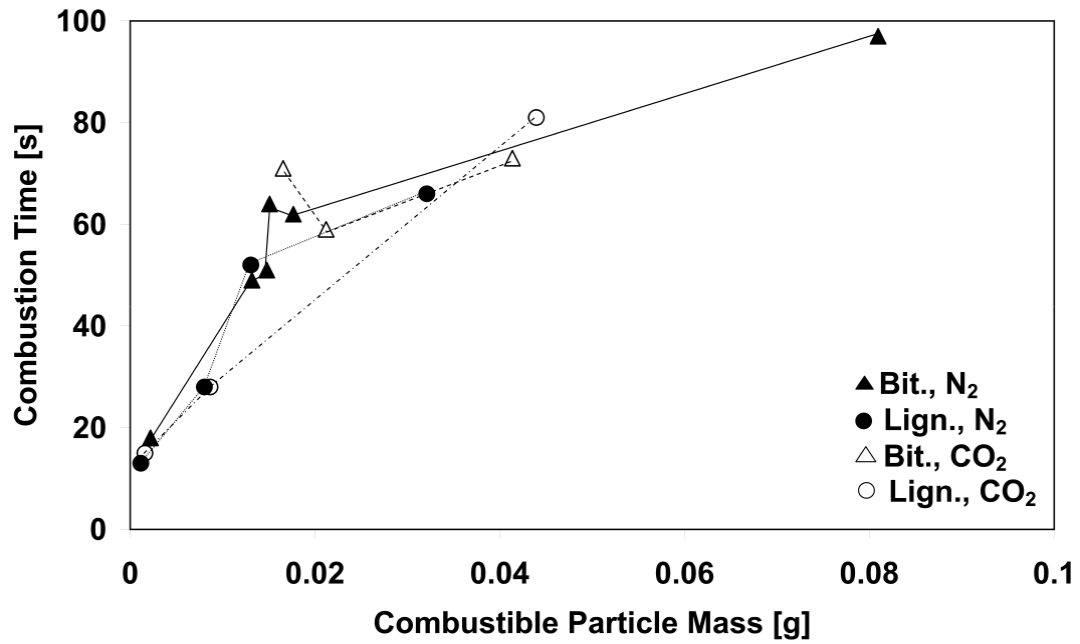


Figure 43 Burnout times for single particle combustion at 40 vol. % O<sub>2</sub> as a function of particle mass.  $d_p = 0.71 - 7$  mm.  $T_{\text{reactor}} = 1073$  K.

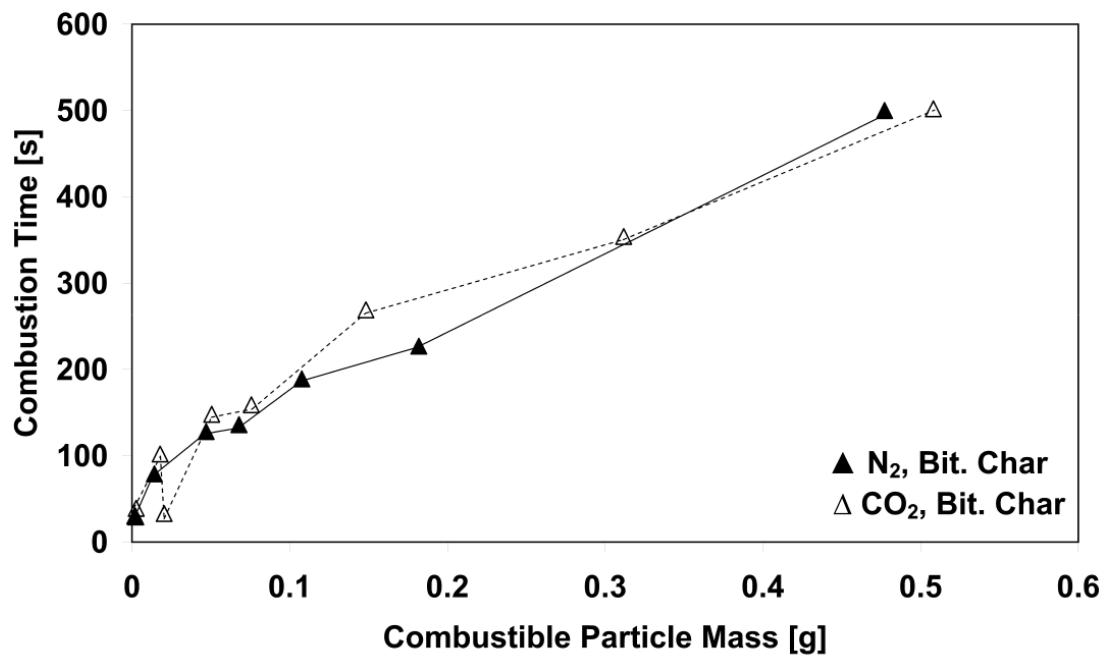


Figure 44 Burnout times for single particle combustion at 30 vol. % O<sub>2</sub> as a function of particle mass.  $d_p = 1.3 - 12.1$  mm.  $T_{\text{reactor}} = 1073$  K.



Camera recordings and visual inspection show that the ash layer remains around the particles after each experiment, which could imply that combustion at lower particle masses is taking place under either kinetic- or external mass transfer control as the burnout time here and in the figures are roughly proportional to  $R_0^{1/3}$  [Levenspiel, 1999]. Considering the high particle temperatures in figure 41 and figure 42 and the trend of lower particle temperatures in  $O_2/CO_2$  in figure 42 it is more likely that external mass transfer affects the combustion rate. This is not unambiguous though since it would then be expected that the burnout times in  $O_2/N_2$  were significantly lower than in  $O_2/CO_2$ , which is not supported by figure 43 and figure 44. Gasification of the char by  $CO_2$  could however contribute to char consumption in  $O_2/CO_2$  thereby lowering the observed burnout time, at least for the highly reactive lignite. As the particle mass increases further the steepness of the profiles in figure 43 and figure 44 reduces and is roughly proportional to  $R_0^{2/3}$ , indicating that the combustion regime is changing to ash diffusion control. The proportionality between burnout time and particle size has been reported previously for similar sized particles [Blackham et al., 1994]. The explanation of figure 41 - figure 44 above should not be taken as unambiguous as the theory presented has not been validated by detailed calculations. This type of discussion does however show the important contribution that the NIR CCD camera recordings brings to the evaluation of experimental data, as the determination of particle temperatures and burnout times in  $CO_2$  environments would not have been possible without the use of the IR-technique.

## 5 Main Conclusions and Recommendations

This report, which concludes PSO-project 010069, has presented result on temperature- and concentration measurements obtained with IR- and FTIR-methods in pilot- and laboratory scale reactors used for combustion experiments under both ordinary combustion and oxy-fuel conditions.

The first part of the report dealing with IR- and FTIR-measurements in a 30 kW down-fired swirl burner has shown that the use of the miniature FTIR probe can be used to obtain temperature profiles with an accuracy (defined as being as close as possible to in situ conditions) as good or better than with a conventional S-type thermocouple. A special advantage is that the method measures the fast fluctuations caused by turbulence and fuel feed flow variations which would be dampened by the use of a shielded thermocouple. It is considered not possible (or at least very difficult) to use a suction pyrometer as ash and fuel particles would quickly plug the probe.

Two features of the FTIR probe limited the accuracy compared to measurements in a full scale boiler. As the diameter of the pilot scale burner was significantly smaller than that of an industrial boiler the optical path length used in the FTIR measurements had to be reduced from 100 – 250 mm down to 30 mm. As the interpretation of the measured emissions into species concentrations and gas temperature are based on the assumption of a homogeneous, well mixed gas phase it meant that mixing limitations and phenomena such as eddies and general turbulent structures at scales smaller than the optical path length caused fluctuations in the data time series. The influence of these possible sources of uncertainty was especially observed near and in the flame and in reality simply reflects the actual conditions in a flame, meaning that the possibility to measure these fluctuations can be seen as a strength of the FTIR technique.

When measurements were carried out during air-blown combustion the beam stop had to be removed to ensure a strong enough signal for temperature determination due to the lower concentration of CO<sub>2</sub> under these conditions compared to oxy-fuel firing. The removal of the beam stop meant that species concentrations of H<sub>2</sub>O, CO<sub>2</sub> and CO could not be determined as the interpretation of their transmittance bands into concentrations where done by Beer's law and therefore relied on a fixed traversed path length of the

signal. Risø-DTU has started the design work for a new miniature FTIR probe with a short path length and build-in IR-source for improved performance in small flames in future projects.

A second “disturbance” in the FTIR-measurements was the cooling effect of the beam stop. This cooling effect meant that gas temperatures measured with the beam stop in place was lower than gas temperatures measured with the beam stop removed and were more in line with measurements obtained with an S-type thermocouple. The S-type thermocouple was also cooled, however, due to radiation from the reactor wall.

The use of the IR camera to measure particle temperatures and determine particle sizes and distributions during experiments in the swirl burner was successful. The only significant error was in the data analysis where dense particle clouds or optical disturbances could be interpreted as large particles by the software. These sources of errors can however be omitted for the use of the technique in future investigations. Because the IR-camera only can see objects hotter or colder than the background, particles having a temperature close to that of the background were not included in the results. If it is possible in future investigations a controlled background, e.g. a window, placed directly opposite the camera would eliminate this problem.

Both the data obtained by IR- and FTIR measurements in the swirl burner will be a valuable contribution in future CFD modeling.

When a NIR CCD camera was used to detect and record particle temperatures in a laboratory scale fixed bed reactor it proved both accurate and useful for interpretation of the data. The ability to evaluate combustion times in  $O_2/CO_2$ , where the high  $CO_2$  concentrations makes impossible to do so from the carbon balance, allowed for a detailed discussion on combustion rate and regime. The film recordings, made up of lumped thermal images, opened for the evaluation of combustion behavior following ignition and showed an explosive behavior of particles burned at high concentrations of  $O_2$ . These kinds of observations are crucial for future modeling work of single particle combustion.

## 6 References

**[Bak & Clausen, 2002]:** J Bak, S Clausen, FTIR emission spectroscopy methods and procedures for real time quantitative gas analysis in industrial environments, Meas. Sci. Technol., 2002 (13) , p. 150-156.

**[Blackham et al., 1994]:** Blackham AU, Smoot LD, Yousefi P, Rates of oxidation of millimetre-sized char particles: simple experiments, Fuel, 1994 (73), p. 602-612.

**[Brix et al., 2010]:** Brix J, Jensen PA, Jensen AD, Coal devolatilization and char conversion under suspension fired conditions in O<sub>2</sub>/N<sub>2</sub> and O<sub>2</sub>/CO<sub>2</sub> atmospheres, Fuel, 2010 (89), p. 3373-3380.

**[Clausen, 1996]:** S Clausen, Local measurement of gas temperature with an infrared fibre-optic probe, Meas. Sci. Technol., 1996 (7), p. 888-896.

**[Molina & Shaddix, 2007]:** Molina A, Shaddix CR, Ignition and devolatilization of pulverized bituminous coal particles during oxygen/carbon dioxide coal combustion, Proc. Combust. Inst., 2007 (31), p. 1905-1912.

**[Liu et al., 2005]:** Liu H, Zailani R, Gibbs BM, Comparisons of pulverized coal combustion in air and in mixtures of O<sub>2</sub>/CO<sub>2</sub>, Fuel, 2005 (84), p. 833-840.

**[Levenspiel, 1999]:** Levenspiel O, Chemical Reaction Engineering, 3rd ed. John Wiley & Sons, Inc, 1999

**[Toftegaard et al., 2010]:** MB Toftegaard, J Brix, PA Jensen, P Glarborg, AD Jensen, Oxy-fuel combustion of solid fuels, Prog. Eng. Combust. Sci., 2010 (36), p. 581-625.

**[Yin et al., 2008]:** C Yin, L Rosendahl, SK Kær, S Clausen, SL Hvid, T Hille, Mathematical modelling and experimental study of biomass combustion in a thermal 108 MW grate-fired boiler, Energy Fuels, 2008 (22), p. 1380-1390.